1

Synthetic Aperture Radar Imaging

1.1. Introduction

Synthetic aperture radar (SAR) imaging, is a technique that allows us to remotely map the reflectivity of objects or environments with high spatial resolution, through the emission and reception of electromagnetic (EM) signals. Images obtained this way can be used for numerous applications, ranging from basic radar (an acronym for radio detection and ranging) functionalities, which are the detection of objects and their geographical localization, including the estimation of some geophysical properties of complex environments, such as certain dimensions, moisture content, roughness, density, etc. Owing to the frequency domains that are generally used by SAR devices, this active sensing system is independent of Sunlight conditions and is very weakly impacted by weather conditions. SAR systems mounted on airborne or satellite sensors rapidly image vast environments that are potentially difficult to access from field measurements. These characteristics make radar imaging systems a tool that is particularly well suited for remote sensing and they are used for a large number of applications in numerous sectors, such as geophysics, defense, environment surveillance, etc.

SAR imaging was first developed in the 1950s, following the initiative carried out by Carl Wiley and his team [WIL 85] who described the technique as antenna beam sharpening in the Doppler domain: the coherent combination of measurements taken by a moving radar allows us to

---

Chapter written by Laurent FERRO-FAMIL and Eric POTTIER.

synthesize an EM map with a better resolution than that of a fixed radar. SAR imaging may be considered as the joint processing of data acquired by an antenna array, whose size can reach several kilometers, and is artificially synthesized by simply moving the measurement platform. Airborne systems were then developed in the 1960s, mainly intended for defense related applications [LAS 05]. During the 1970s, the use of SAR technology for civilian applications, with projects related to oceanography, led to the development of the first SAR satellite, SEASAT, which alongside its successors, SIR-A and SIR-B, provoked a very pronounced interest from the scientific community [OUC 13]. Numerous missions and satellite projects have been carried out since the end of the 1980s, largely demonstrating the potential of SAR technology for the remote sensing of the terrestrial environment. The advent of recent sensors operating at a sub-metric resolution, such as TerraSAR-X and COSMO-SkyMed, or with very high temporal resolution, such as Sentinel-1, and a series of systems ensuring continuous measurements over several decades, allow us to consider the operational applications amongst a large number of civilian sectors, such as environmental surveillance, security of goods and people and many other fields in geophysical sciences.

This chapter aims to provide the reader with a description of the basic principles of radar imaging and the fundamental analysis necessary for interpreting SAR images. Section 1.2 provides an introduction to SAR imaging and presents, after a brief review of different mechanisms related to the propagation of EM waves and their interaction with matter, a simple model for a signal measure by a radar, based on the first-order Born approximation is given. It is then shown, in an informal manner, that the use of measurements taken with frequency or spatial diversity allow us to consider the inversion of the signal model, in other words, the localization of the different scatterers measured and the estimation of their reflectivity that form the fundamental objective of SAR imaging. This section is followed by a presentation of the principle of range signal focusing using a spectral diversity, using various waveforms commonly used by modern radars. The synthesis of the SAR images using spatial diversity, for which we introduce a 2D focusing technique based on back projection, which is iterative and intuitive, is then presented and completed by a review of different constraints ruling the main parameters of an SAR system. Section 1.3 presents a description of general characteristics of SAR images acquired over environments and the processing steps required for interpreting their content. We first show the sensitivity of SAR radiometry to the spectral

domain used during the acquisition, to the type of environment observed and to the EM scattering mechanisms occuring during interactions between radar wave and matter. The speckle effect, inherent to the use of a coherent system, is described and analyzed in terms of statistical properties of the focused signal and different speckle filtering techniques, based on the estimation of incoherent second-order moments, which are then detailed. This section follows with a presentation of detailed geometric properties characteristic of SAR imaging and the influence of spatial resolution on the interpretation of an image's informational content. This section concludes with a description of spaceborne SAR's main modes of measurement, which propose different ways of managing the physical compromise between resolution and the spatial coverage of an image, for which limitations arise in relation with the characteristics of a radar system. Section 1.4 concerns the calibration of SAR images and the correction of errors, related to the imperfections and temporal variations of the radar system's features.

1.2. Introduction to synthetic aperture radar (SAR) imaging

1.2.1. *Objectives of a coherent radar measurement*

The principle of a measurement made by an active radar is illustrated in Figure 1.1. A radar emits an electromagnetic (EM) wave that propagates within a certain domain of space and measures the response of an obstacle, also called target or scatterer. The analysis of the signal received, $s_r(\tau)$, allows us to estimate some geophysical properties of the illuminated object, such as, for example, its EM reflectivity, through the energy of the measured signal, or the radar-target distance, which is a function of τ_0, the time taken for the wave to travel from the radar to the target and back again [SKO 08].

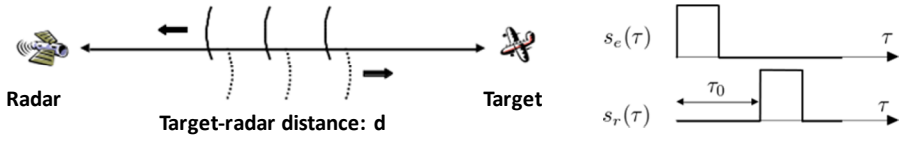

Figure 1.1. *Principle of a radar measurement, with $s_e(\tau)$ being the emitted signal and $s_r(\tau)$ being the response of an object*

As is shown hereinafter, the use of some physical elementary principles related to the propagation of the EM waves and their interaction with matter, allows us to formulate a simple and generic expression of the signal received by the radar, which may be used as a base model to synthesize EM images.

1.2.1.1. *The concept of EM wave propagation*

The behavior of an electromagnetic field is fully described by the Maxwell equations, where all quantities are a function of time, t, and of the spatial position considered, $\boldsymbol{r} = (x, y, z)$:

$$\vec{\nabla} \times \vec{\mathrm{E}} = -\frac{\partial \vec{B}}{\partial t}, \vec{\nabla} \times \vec{\mathrm{H}} = \vec{J} + \frac{\partial \vec{D}}{\partial t}, \vec{\nabla} \cdot \vec{\mathrm{D}} = \rho, \vec{\nabla} \cdot \vec{B} = 0 \qquad [1.1]$$

where $\times$ and $\cdot$ respectively represent the vector and scalar product, $\vec{\nabla} = \left[\frac{\partial}{\partial x} \frac{\partial}{\partial y} \frac{\partial}{\partial z}\right]^T$ in Cartesian coordinates, and with $\vec{E}$, the electric field, $\vec{H}$, the magnetic field, $\vec{B}$, the density of magnetic flux, $\vec{D}$, the density of electric flux, ρ, the density of free charge, and $\vec{J}$, the density of free current. We consider a linear medium, where the fields and flux densities can be linked as $\vec{D} = \epsilon \vec{E}$ and $\vec{B} = \mu \vec{H}$, with ϵ the electric permittivity and μ the magnetic permeability of the medium. In addition, assuming that the medium does not contain a free source, $(\rho = 0, \vec{J} = \vec{0})$, we obtain, using [1.1] a homogeneous equation of propagation, for $\vec{E}$ and $\vec{B}$ given by:

$$\vec{\nabla}^2 \vec{\mathrm{E}} - \epsilon\mu \frac{\partial^2 \vec{E}}{\partial t^2} = \vec{0} \qquad [1.2]$$

with $\vec{\nabla}^2$ the vectorial Laplacian operator, defined in Cartesian coordinates, as $\vec{\nabla}^2 \vec{\mathrm{E}} = \frac{\partial^2 \vec{\mathrm{E}}}{\partial x^2} + \frac{\partial^2 \vec{\mathrm{E}}}{\partial y^2} + \frac{\partial^2 \vec{\mathrm{E}}}{\partial z^2}$.

Amongst the infinite number of solutions to [1.2], we can cite two types of useful progressive waves are generally considered for modeling a radar measurement – the spherical symmetric wave and the plane wave.

1.2.1.1.1. Propagation of a spherical wave

We consider a wave created by a monochromatic source, with pulsation ω_c, placed at O, the center of the coordinate system $(\hat{x}, \hat{y}, \hat{z})$, and radiating an

electromagnetic field in an isotropic way. The solution of the corresponding propagation equation is given in spherical coordinates, $(\hat{r}, \hat{\theta}, \hat{\phi})$, by:

$$\vec{\mathrm{E}}(\boldsymbol{r}, t) = \vec{\mathrm{E}}_0 \frac{e^{j(\omega_c t - \kappa_c r)}}{r}, \text{ with } \vec{\mathrm{E}}_0 = \begin{bmatrix} 0 \\ E_\theta e^{j\xi_\theta} \\ E_\phi e^{j\xi_\phi} \end{bmatrix} \text{ and } \kappa_c = \sqrt{\mu\epsilon}\,\omega_c \quad [1.3]$$

where $\vec{E}(\boldsymbol{r}, t)$ represents the complex value of the analytical signal, of the real electric field, $\vec{E}_{\mathcal{R}}(\boldsymbol{r}, t) = Re\left(\vec{E}(\boldsymbol{r}, t)\right)$, and $\kappa_c = \frac{2\pi}{\lambda_c}$ is the wave number, with λ_c, the associated wavelength. Expression [1.3] shows that the electric field propagates in a radial direction, $\hat{r}$, at a velocity of $v = \frac{\omega_c}{\kappa_c} = \frac{1}{\sqrt{\mu\epsilon}}$, with an amplitude that decreases proportionately to the radial position r. The nullity of the radial components of both $\vec{E}(\boldsymbol{r}, t)$ and $\vec{B}(\boldsymbol{r}, t)$, verified for an isotropic medium, is characteristic of a transverse EM wave, having fields that are orthogonal to the direction of propagation, and to each other. This solution can be expanded to non-monochromatic waves, i.e. having a non-null spectral content within a band that includes the carrier frequency f_c, such as $\vec{E}(\boldsymbol{r}, t) = u(t)\vec{E}_0 \frac{e^{j(\omega_c t - \kappa_c r)}}{r}$, $u(t)$ being a baseband signal with a spectrum $U(f)$ that covers a spectral domain width B_f. For a non-dispersive medium, i.e. when ϵ and μ remain unchanged on the covered spectral band, the propagation characteristics of this wave are identical to those of an EM monochromatic signal, and the emitted signal is not deformed during propagation. We can note that this type of wave is not physically achievable, but it represents a good approximation for the field radiated by a small dipole and can be used to model the wave by a radar a long distance from it.

1.2.1.1.2. Propagation of a plane wave

A plane wave is a solution of the propagation equation that propagates in an direction orthogonal to a plane, with normal $\hat{\boldsymbol{\kappa}}$, and its electric field is $\vec{E}(\boldsymbol{r}, t) = \vec{E}_0 e^{j(\omega_c t - \kappa_c \hat{\boldsymbol{\kappa}}.\boldsymbol{r})}$, with $\vec{E}_0$ such that $\vec{E}_0.\hat{\boldsymbol{\kappa}} = 0$. Contrary to the previous case, the wave presents constant amplitude and phase on a plane orthogonal to $\hat{\boldsymbol{\kappa}}$. The example in Figure 1.2, for which $\hat{\boldsymbol{\kappa}} = \hat{\boldsymbol{z}}$, shows the trajectory followed by the electric field, characteristic of the wave polarization state, that can, depending on the

relative amplitudes and phases of the components of $\vec{E}_0$ corresponding to directions $\hat{\boldsymbol{x}}$ and $\hat{\boldsymbol{y}}$, be linear, circular or, more generally, elliptical.

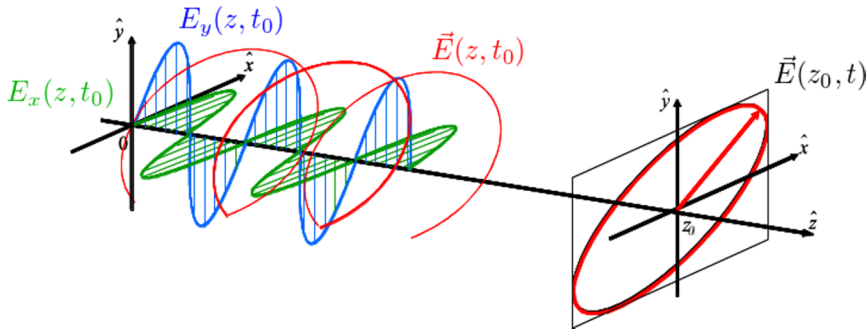

Figure 1.2. *Representation of an elliptically polarized plane wave. The electric field follows a helicoidal spatial trajectory and an elliptical temporal trajectory*

The plane wave represents a solution for the propagation equation that can be easily handled and is largely used to simulate the response of objects or to interpret complex phenomena linked to the interaction between wave and matter, mainly because of its local relationship with the more general spherical solution. This relationship is illustrated in Figure 1.3(b), with a virtual object of size D, illuminated by a spherical wave at a distance r_0 from the emitter, relatively large compared with the object's dimension. The spherical wavefront can be approximated locally by a plane wave, defined by the plane, tangent to the sphere with a radius r_0 and propagates in an direction orthogonal to this plane. The validity of this approximation is generally evaluated using an empirical criterion, known as the far field criterion, given by $r_0 > \frac{2D^2}{\lambda_c}$, with $r_0, D \gg \lambda_c$, and D, the radius of the sphere including the measured object [KNO 74]. This criterion corresponds to an arbitrary phase error criterion given by $|\Delta\phi| = \frac{2\pi}{\lambda_c}\Delta d < \frac{\pi}{8}$. When this criterion is verified, the EM radiation from the object can be accurately approximated by its response to a plane wave, which is generally much easier to simulate or calculate. Finally, we can note that a spherical wave can be decomposed by means of an inverse Fourier transformation, as a sum of plane waves, $\psi(\boldsymbol{r}) = \frac{e^{jk_h r}}{r} = \frac{1}{4\pi^2}\int \frac{1}{k-k_h} e^{j\boldsymbol{k}.\boldsymbol{r}} d\boldsymbol{k}$, as is illustrated in Figure 1.3(c).

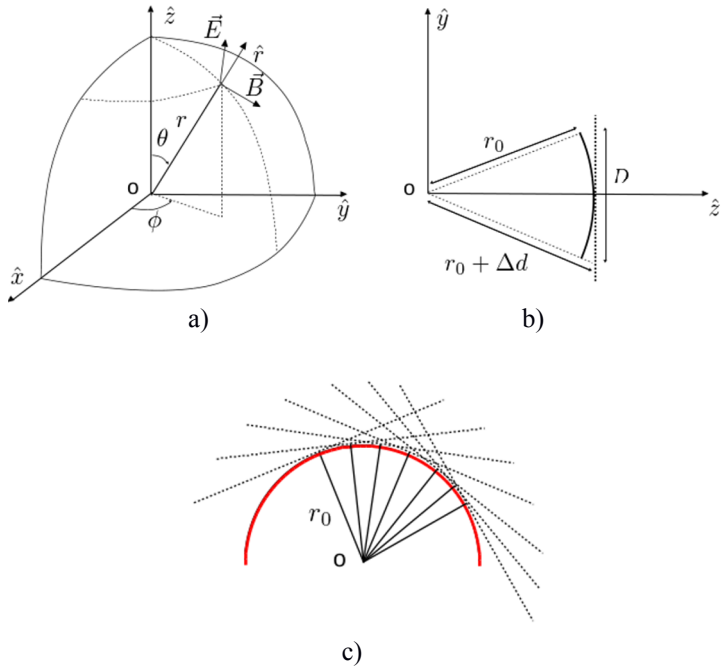

Figure 1.3. *a) Representation of the EM field of a spherical wave at the coordinates (r, θ, ϕ), b) local approximation of a spherical wave by a plane wave, c) decomposition of a spherical wave into a sum of plane waves*

1.2.1.2. *Modeling the radar response of an object*

1.2.1.2.1. Elementary interactions between an EM wave and an environment

The interaction of the EM wave with an environment can be briefly described by four elementary mechanisms, illustrated in Figure 1.4, reflection, refraction, diffraction and scattering [ISH 99, TSA 00, ULA 81, ULA 82, ULA 86]. A wave illuminating a homogeneous medium, whose dimensions are large compared to wavelength, is partially reflected at an interface corresponding to the contour of the medium. We can distinguish specular reflection over smooth interfaces, and the diffuse reflection over rough surfaces. The refraction phenomenon is typical of wave propagation through an interface that separates two mediums with different dielectric dielectric characteristics. The propagation from one medium to another is accompanied by a modification of the wave velocity and by a change in the

direction of propagation. Diffraction is a phenomenon that occurs when illuminating an object that has a comparable size to the wavelength used. The target, which represents a strong discontinuity, radiates a field, composed of a superposition of a large number of terms, which possesses very pronounced directional features. The last elementary interactional mechanism is EM diffuse scattering, which occurs when a wave propagates in a host medium containing heterogeneities, i.e. arbitrarily sized particles with their own physical characteristics, different from those of their host medium. Each particle radiates a field, in all spatial directions, weighted by its own radiation diagram and all of the contributions interact with one another. As is shown in Figure 1.4, these different phenomena generally coexist when a realistic medium, having complex scattering characteristics, is illuminated.

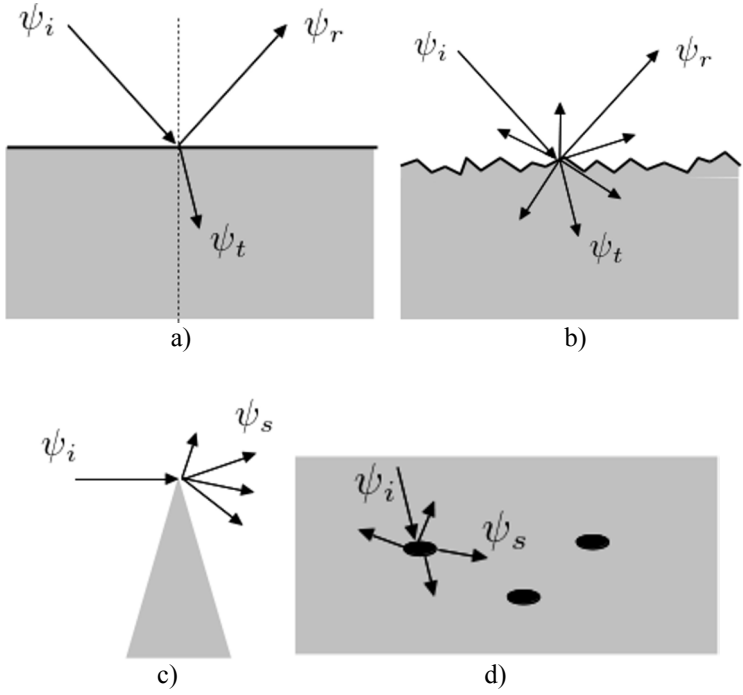

Figure 1.4. *Illustration of the interaction between an incident wave ψ_i and matter, generating a reflected wave, ψ_r, a refracted wave, ψ_t, a diffracted or scattered wave, ψ_s. Elementary mechanisms: reflection–refraction on an interface, that is: a) smooth; b) rough; c) diffraction; d) scattering*

1.2.1.2.2. First-order Born approximation

We consider a non-dispersive and dielectric host medium, within which a scalar wave, $\psi(\boldsymbol{r})$, propagates, which interacts with heterogeneities that may be dialectic, partially or totally conducting. In this case, the propagation equation given by [1.2] is no longer homogeneous and may be expressed using complex notation, as:

$$\nabla\psi(\boldsymbol{r}) - k_h^2\psi(\boldsymbol{r}) = f(\boldsymbol{r})\psi(\boldsymbol{r}) \qquad [1.4]$$

where $f(\boldsymbol{r})$ is called the scalar potential of the scattering medium and represents its radiation features. The total field is expressed as $\psi(\boldsymbol{r}) = \psi_h(\boldsymbol{r}) + \psi_s(\boldsymbol{r})$, where $\psi_h(\boldsymbol{r})$ represents a solution to the homogeneous equation and $\psi_s(\boldsymbol{r})$ is a solution to the complete equation. It can be shown that this latter term can be expressed as a convolution with the Green's function of the medium, the solution of [1.4] with $f(\boldsymbol{r}) = \delta(\boldsymbol{r})$, so that:

$$\psi(\boldsymbol{r}) = \psi_h(\boldsymbol{r}) + \psi_s(\boldsymbol{r}) = \psi_h(\boldsymbol{r}) + \int_V f(\boldsymbol{r}')\,\psi(\boldsymbol{r}')\frac{e^{j\kappa_h|\boldsymbol{r}-\boldsymbol{r}'|}}{|\boldsymbol{r}-\boldsymbol{r}'|}\,d\boldsymbol{r}' \qquad [1.5]$$

During a radar measurement, $\psi_h(\boldsymbol{r})$ represents the incident wave emitted by the radar and $\psi_s(\boldsymbol{r})$ symbolizes the wave scattered by the heterogeneities of the volume V. The resolution of [1.5] is generally difficult due to the presence of the total wave, $\psi(\boldsymbol{r}')$, inside the volumetric integration. Given the weakly scattering heterogeneities assumption, i.e. the scattered field is weak in comparison with the incident field, $|\psi_s(\boldsymbol{r})| \ll |\psi_h(\boldsymbol{r})|$, we can apply a first-order approximation by replacing $\psi(\boldsymbol{r}')$ by $\psi_h(\boldsymbol{r}')$ in the integration of [1.5] [ISH 99, TSA 00, ULA 86]. The consequence of this approximation can be formalized by considering a set of scalar potentials representing spatially isolated heterogeneities, illuminated by the incident wave:

$$f(\boldsymbol{r}) = \sum_i f_i(\boldsymbol{r}) \quad \Rightarrow \psi(\boldsymbol{r}) = \psi_h(\boldsymbol{r}) + \sum_i \psi_{s_i}(\boldsymbol{r}) \qquad [1.6]$$

The total scattered field is simplified as a sum of individual contributions that, may be adjusted in order to account for certain local propagation effects on the incident field such as refraction and attenuation, but cannot take into account the mutual interactions between several sources of scattering. For this, we can consider additional order-n terms, from the integral in [1.5] and for which we would replace $\psi(\boldsymbol{r})$ by the term $\sum_i \psi_{s_i}(\boldsymbol{r})$ obtained

from the order $n-1$. The principle of the first-order Born approximation is illustrated in Figure 1.5.

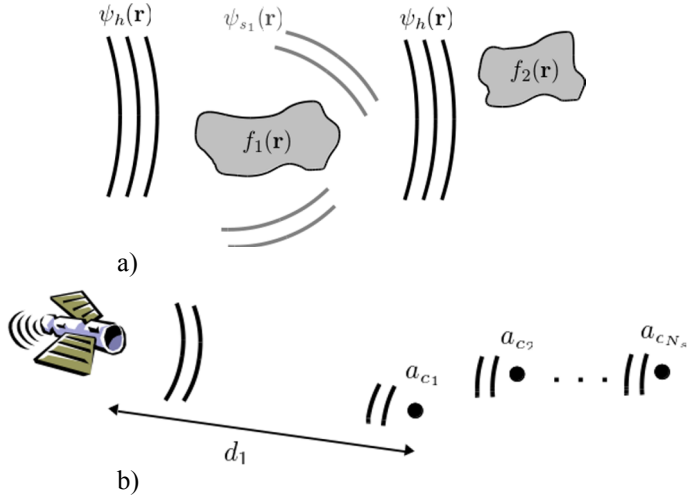

Figure 1.5. *Illustration of the first-order Born approximation. a) The wave interacting with $f_i(\boldsymbol{r})$ is approximated by $\psi_h(\boldsymbol{r})$, b) a radar measurement from a discrete scene that does not account for multiple interactions*

1.2.1.2.3. Linear model of a signal measured by a radar

The generic architecture of a coherent radar, that measures the signal phase, is illustrated in Figure 1.6 [SKO 08, FER 14]. The baseband waveform used by the radar, $u(\tau)$, is transposed, by multiplication or by mixing with the carrier signal, $e^{j\omega_c\tau}$, in the radiofrequency (RF) spectral domain, centered around the pulsation ω_c. After amplification of the modulated signal, $p(\tau)$, the emitted RF signal, $s_{e_{RF}}(\tau)$, is converted into an EM field and transmitted by the emitting antenna. The receiving antenna measures and converts the field scattered by the scene observed into a RF signal, $s_{r_{RF}}(\tau)$, which is then transposed into baseband, using the conjugate carrier signal, to retrieve the received signal, $s_r(\tau)$, that is then digitized and saved before processing. The fundamental characteristics of a coherent radar system are the carrier frequency and waveform used, the configuration of the antenna system and the quality of the signal received, generally quantified with the signal to noise power ratio (SNR).

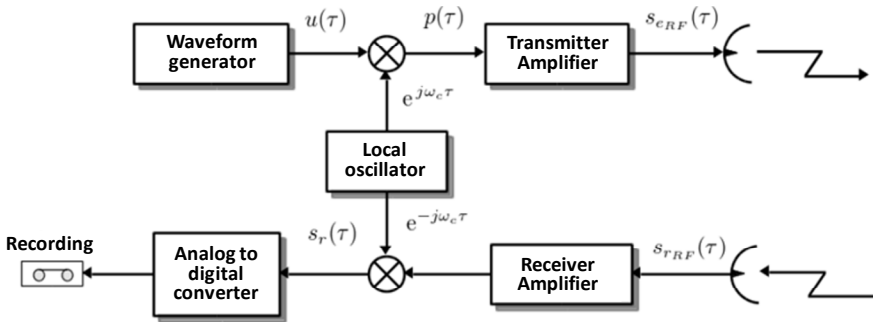

Figure 1.6. *Synopsis of a coherent radar system*

A radar is generally considered to be a system with co-localized emission and reception, i.e. waves are emitted and received at the same physical location, which may be considered as a point-like source. The emitted spherical wave propagates from position $\boldsymbol{r}_0$, in a non-dispersive host medium, at a velocity $c = \frac{\omega_c}{\kappa_c} = \frac{1}{\sqrt{\mu_0 \epsilon_0}}$. In order to limit the complexity of the signal expressions, we consider, without real loss of generality, a typical scene described by Figure 1.5(b), and comprising a set of N_s point targets, with non-dispersive reflectivity in the considered band, $f(\boldsymbol{r}) = \sum_{i=1}^{N_s} f_i\, \delta(\boldsymbol{r} - \boldsymbol{r_i}) \in \mathbb{C}$, and positioned at the spherical coordinates $(d_i = \|\boldsymbol{r}_0 - \boldsymbol{r_i}\|, \theta_i, \phi_i)$, with respect to the radar. In the case of a single target observed, $N_s = 1$, the incident wave interacting with the target is given by $\psi_h(\boldsymbol{r_1}, \tau) = g_e(\theta_1, \phi_1) \frac{s_{e_{RF}}\left(\tau - \frac{d_1}{c}\right)}{d_1}$, with $g_e(\theta_1, \phi_1)$, the conversion factor of the emitting antenna, and gives way to a scattered spherical wave, $\psi_{s_1}(\boldsymbol{r_1}, \tau) = f_1\, \psi_h(\boldsymbol{r_1}, \tau)$, which after propagation to the radar, is converted by the receiving antenna into an RF measured signal, given by, $s_{r_{RF}}(\tau) = g(\theta_1, \phi_1)\, f_1 \frac{s_{e_{RF}}\left(\tau - \frac{2d_1}{c}\right)}{d_1^2} \triangleq a_{c_1} s_{e_{RF}}\left(\tau - \frac{2d_1}{c}\right)$, where $g(\theta_1, \phi_1)$ represents the conversion factor of the antenna system for the considered direction. By applying the first-order Born approximation, we find in the case of N_s targets, $s_{r_{RF}}(\tau) = \sum_{i=1}^{N_s} a_{c_i} s_{e_{RF}}(\tau - \tau_i)$. After coherent demodulation, the signal received baseband is expressed as:

$$s_r(\tau) = \sum_{i=1}^{N_s} a_{c_i} u(\tau - \tau_i)\, e^{-j\omega_c \tau_i} \text{ with } \tau_i = \frac{2d_i}{c} et\ d_i = \|\boldsymbol{r}_0 - \boldsymbol{r_i}\| \qquad [1.7]$$

The aim of a radar measurement is to inverse the simple linear model expressed in [1.7], i.e. to estimate the equivalent reflectivity, a_{c_i} or $|a_{c_i}|$, and the radial position, d_i, of each target [SOU 99].

The response from a scene comprising a continuum of non-separable scatterers is described through the use of a coherent reflectivity density rather than from using a set of point-like contributions. The model of the received signal is thus expressed as:

$$s_r(\tau) = \int_W a_c(\boldsymbol{r}')\, u(\tau - \tau')\, e^{-j\omega_c \tau'} J(d', \tau')\, \mathrm{d}V'$$

with

$$\tau' = \tfrac{2d'}{c} \text{ et } d' = \|\boldsymbol{r}_0 - \boldsymbol{r}'\| \qquad [1.8]$$

where $a_c(\boldsymbol{r}')$ represents the equivalent of coherent reflectivity density, measured in the illuminated volume, W and $J(d', \tau')$ is the Jacobian relative to the transformation of distance into time. Expression [1.8] is more general than [1.7], found with a discrete model, $a_c(\boldsymbol{r}) = \sum_{i=1}^{N_s} a_{c_i}\, \delta(\boldsymbol{r} - \boldsymbol{r}_i)$. Despite this parallel, the responses of a distributed medium and of point scatterers have different statistical behaviors. The response of a point scatterer such as a calibration target is deterministic by nature. Distributed environments are formed by a very large number of scatterers having EM characteristics that are generally independent. The superposition of the different contributions of scatterers confer to $a_c(\boldsymbol{r})$ a random aspect called speckle. By virtue of the central limit theorem, applicable to homogeneous environments, $a_c(\boldsymbol{r})$ follows a circularly complex Gaussian distribution, having a zero mean value and a variance equal to $\sigma_a^2(\boldsymbol{r})$. The density, $a_c(\boldsymbol{r})$, is generally considered as being spatially white, i.e. formed of decorrelated spatial samples at the scale of analysis.

1.2.1.2.4. Power budget

The signal actually received by a radar system, $s_{r_n}(\tau) = s_r(\tau) + n(\tau)$, is formed of a useful component, $s_r(\tau)$, which can be modeled as shown by [1.7] or [1.8], and by a measurement noise, inherent to the use of electronic devices, and random by nature, $n(\tau)$. The quality of the received signal may be measured through the ratio of powers associated with the useful component and with noise, called the signal to noise power ratio, $SNR = \frac{P_r}{P_n}$.

The expression of the average power received, for a scatterer located at a distance d and in a direction (θ, ϕ) from the radar, is given by [CUR 91]:

$$P_r = \frac{P_e G_e(\theta,\phi)}{4\pi d^2}\sigma(\theta,\phi)\frac{1}{4\pi d^2}A_r(\theta,\phi) = \frac{P_e G_e(\theta,\phi)G_r(\theta,\phi)\lambda^2\sigma(\theta,\phi)}{(4\pi)^3 d^4} \quad [1.9]$$

where P_e represents the average power of the emitted wave, and $G_e(\theta,\phi)$ or $G_r(\theta,\phi)$, the gain for the emitting or the receiving antenna. The radiation characteristics of an antenna are defined by its gain, $G(\theta,\phi)$, which is computed as the ratio between the radiated power surface density at a distance d from the antenna, $I(d,\theta,\phi)$, in $\mathrm{W/m^2}$, and that radiated by an isotropic antenna, $I_{iso}(d)$, uniformly distributed on a sphere with radius d, $G(\theta,\phi) = \frac{I(d,\theta,\phi)}{I_{iso}(d)} = \frac{4\pi}{\lambda^2}A_e(\theta,\phi)$, with $I_{iso}(d) = \frac{P_e}{4\pi d^2}$, where P_e represents the power of the wave radiated by the antenna. The gain can also be expressed using A_e, in m^2, the antenna's effective area. The central expression of [1.9] is composed of four distinct terms associated with specific quantities. The first represents the power surface density radiated by the transmitter, $I(d,\theta,\phi)$, expressed at the location of the scatterer, i.e. at a distance d from the radar. The second term associated with the response of a scatterer is modeled by $\sigma(\theta,\phi)$ in m^2, the radar cross section (RCS), which receives part of the incident power density, as does an antenna with an equivalent area σ, before radiating it towards the radar. The third term represents the wave attenuation caused by symmetric spherical propagation from the scatterer to the radar, and the last term, $A_r(\theta,\phi)$, indicates the effective surface of the receiving antenna that captures part of the backscattered power density, to convert it into the power received, P_r. The RCS is a characteristic of the observed scatterer and can be expressed as a function of the reflection coefficient $\sigma(\theta,\phi) = \lim_{d\to+\infty} 4\pi d^2 \frac{|E_S(d)|^2}{|E_i|^2}$, where $E_s(d)$ represents the amplitude of the reflected field from the scatterer at a distance d away from it, in other words at the receiving antenna, and E_i is the incident field at the level of the scatterer.

An illustration of the different terms needed to determine the power received by the radar for a bistatic configuration measurement, i.e. when the transmitter and the receiver are not co-localized, is shown in Figure 1.7.

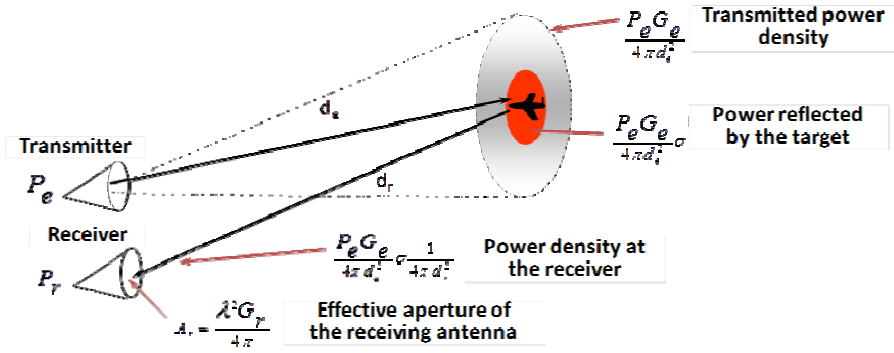

Figure 1.7. *Illustration of the different components of the power expression received for a bistatic radar measurement. For a configuration with a co-localized emission and reception, we have:* $d = d_e = d_r$

The complex valued measurement noise, $n(\tau)$, is characterized by a zero mean value and is considered as white on the effective spectral band of the receiver, B_e. It has a uniform power spectral density on this domain equal to N_0, in W/Hz. The sampling of this signal at a frequency $f_s = B_e$ gives uncorrelated samples having a variance equal to $B_e N_0$. The SNR, for a point scatterer, is therefore expressed as [CUR 91]:

$$SNR = \frac{P_e G_e(\theta,\phi) G_r(\theta,\phi) \lambda^2 \sigma(\theta,\phi)}{(4\pi)^3 d^4 B_e N_0} \qquad [1.10]$$

Unlike point-like scatterers that have a deterministic response, distributed media have a reflectivity formulated as $E(\sigma) = \sigma_0\, dA$ with σ_0, a mean spatial density of the RCS, in m^2/m^2, and dA, an elementary surface. The SNR obtained during the observation of the surface A is expressed as [CUR 91]:

$$SNR = \frac{P_e \lambda^2}{(4\pi)^3 B_e N_0} \int_A \frac{G_e(\theta,\phi) G_r(\theta,\phi) \sigma_0(\boldsymbol{r})}{d^4}\, dA \qquad [1.11]$$

which for the case of a surface of small dimensions compared with d and for a uniform reflective density, gives:

$$SNR = \frac{P_e \lambda^2 G_e(\theta,\phi) G_r(\theta,\phi) \sigma_0 A}{(4\pi)^3 d^4 B_e N_0} \qquad [1.12]$$

1.2.1.3. *Principles of radar imaging using diversity*

1.2.1.3.1. Range imaging using spectral diversity

In the trivial case of a scene comprising a single target, $N_s = 1$, the use of a monochromatic wave, with $u(\tau) = 1$, leads to a constant received signal $s_r(\tau) = A\, e^{j\varphi} = a_{c_1} e^{-j\omega_c \tau_1}$, from which we can estimate $|a_{c_1}|$, but which does not allow us to identify d_1, because, in general, $\omega_c \tau_1 \gg 2\pi$ and $a_{c_1} \in \mathbb{C}$. One of the solutions to this limitation uses a spectral diversity, with a polychromatic waveform such as $u(\tau) = e^{-j\Delta\omega\tau} + e^{+j\Delta\omega\tau}$. The spectral separation of the received signals, $s_{r_{\pm\Delta\omega}}(\tau)$, allows us to therefore establish a system of two complex equations and to identify a_{c_1} and d_1 without ambiguity, for a spectral excursion that is sufficiently small, so that $\Delta\omega\, \tau_1 < \pi$. For an arbitrary number of sources, the N_s parameters pairs, (a_{c_i}, d_i), can be estimated with the help of a sufficient number of frequency components, selected in an adequate manner. We therefore use a waveform, $u(\tau)$, with a bandwidth B_f, adapted to the analysis of the observed scene.

1.2.1.3.2. 2D and 3D imaging using spatial diversity and other types of diversity

We can, for the previously cited example, with $N_s = 1$, consider a solution that is different from the one based on spectral diversity. In fact, measurements taken at different positions, sufficiently close enough to avoid ambiguity in the coherent information, generate a phase diversity that can be used to determine the observed target's parameters. This principle can be generalized to an arbitrary number of targets, by means of a sufficient number of positions of measurement. For the measurement of the radial position of an object, d, the use of a spectral diversity is generally preferred, as this mode of diversity is easy to implement, the determination of other spatial coordinates of the measured scatterers, (θ_i, ϕ_i), i.e. 2D or 3D imaging, is generally achieved through the help of 1D or 2D imaging spatial diversity that completes the information obtained by spectral diversity. Other types of diversity (polarization, frequency bands, acquisition time, etc.) can be used to show a type of interaction between waves and matter or to estimate some geophysical parameters with the help of EM response models.

1.2.2. *Range focusing*

1.2.2.1. *Radar waveforms*

The most widely used waveforms that generate the necessary frequency diversity required to discriminate several targets are illustrated in Figure 1.8.

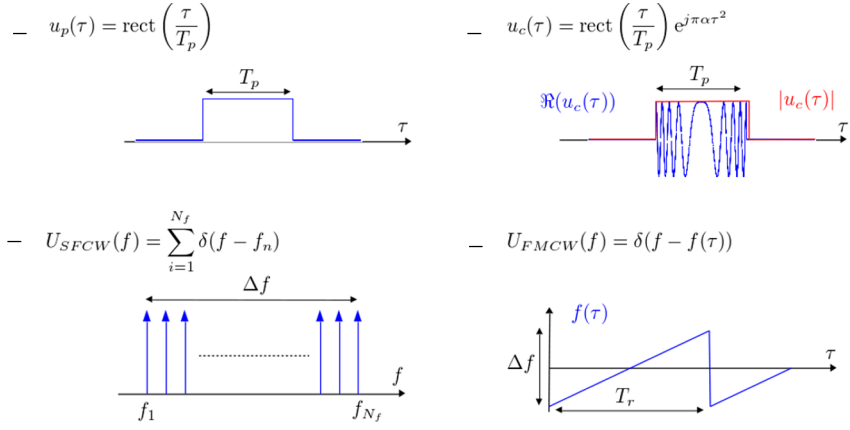

Figure 1.8. *Examples of pulsed radar waveforms*

We can distinguish the pulsed waveforms, $u_p(\tau)$ and $u_c(\tau)$, characterized by a limited temporal support, with a duration of T_p, short compared with the wave's travel time between the radar and the measured object, and continuous waves (CW), defined in the spectral domain [SKO 08, FER 14, SOU 94]. The waveform $u_p(\tau)$ is a classical pulse, whereas $u_c(\tau)$ is a pulse modulated linearly in frequency, generally called a chirp, referencing the chirping of birds that presents similar features. These waveforms having finite durations are directly applicable to the radar response model introduced by [1.7] and [1.8]. The second type of waveform corresponds to "continuous waves", i.e. signals with a constant amplitude in time and with a frequency that varies slowly, or in a discrete way. Stepped frequency continuous waves (SFCW) radar systems measure the steady response of a scene with the help of monochromatic (sinusoidal) signals, and for discrete frequency values, as can be done by a vector network analyzer. The frequency modulated continuous waves (FMCW) technique is the continuous version of this kind of system and is based on a slow scanning, over a duration T_r, of a predefined spectral domain. The pulsed waveforms

mainly differ in their spectral width. The waveform $u_p(\tau)$ possesses a bandwidth given by $\frac{1}{T_p}$, whereas $u_c(\tau)$, with instantaneous frequency $f = \alpha\tau$, has a spectrum given by $U_c(f) \approx rect\left(\frac{f}{B_f}\right) e^{j\pi\frac{f^2}{\alpha}}$, with a width given by $B_f = \Delta f = \alpha\, T_p$, if $\Delta f\, T_p \geq 200$ [CUM 05, FER 14]. These waveforms require an efficient transmitting system with an adapted bandwidth and rise time. In comparison with the pulsed approach, the CW measurement mode, based on slow measurements performed over an equivalent spectral range, allows us to synthesize temporal waveforms $u_{SFCW}(\tau)$ and $u_{FMCW}(\tau)$ assimilable to impulsions, with reduced material complexity.

1.2.2.2. *Range focusing by adapted filtering, resolution and sampling*

1.2.2.2.1. Principle of focusing by adapted filtering

In the presence of a acquired noise and for a discrete scene, the signal received by the radar can be modeled as:

$$s_r(\tau) = \sum_{i=1}^{N_s} a_{c_i} u(\tau - \tau_i)\, e^{-j\omega_c \tau_i} + n(\tau) = s_{r_u}(\tau) + n(\tau) \qquad [1.13]$$

with $s_{r_u}(\tau)$ the useful component of the received signal, and $n(\tau)$ a white noise on the used frequency band, centered and with variance σ_n^2. The potential of differentiation and identification of the different targets measured by a radar is generally quantified through using its range resolution and the SNR of the received signal, which are illustrated in Figure 1.9.

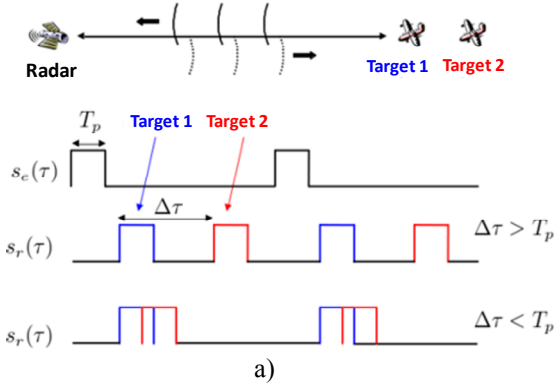

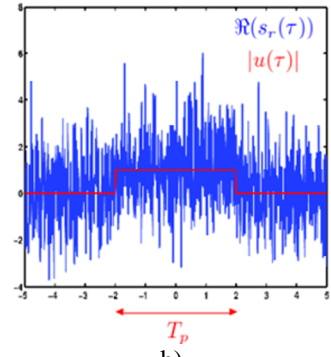

Figure 1.9. *a) Illustration of range resolution; b) an example of a noisy signal received*

The resolution of an imaging system is its capacity to discriminate the responses from scatterers located in neighboring positions. In the case of Figure 1.9(a), the objects' contributions can be differentiated if $\Delta\tau = |\tau_1 - \tau_2| > T_p$. The range resolution, defined as the minimal range between two targets, is therefore given by $\delta d = \frac{c\,T_p}{2}$. The SNR of the received signal is $SNR(\tau) \propto \left|s_{r_u}(\tau)\right|^2 / \sigma_n^2$ and proves to be, in the example in Figure 1.9, insufficient for a precise estimation of the target's parameters. As is shown in Figure 1.10, the range focusing of the measured signal jointly aims to concentrate a scatterer response around its temporal abscissa τ_i and improve the SNR at this position, in order to finally obtain a reliable estimate of the scatterer's reflectivity, $|a_{c_i}|$. It is generally implemented under the form of a linear filtering of the received signal, applicable for discrete or distributed scenes. The focused signal is expressed as $s_{rf}(\tau) = s_r(\tau) * g_r(\tau)$, with * the convolution operator and $g_r(\tau)$ the focusing filter. The model given in [1.13], indicates that focusing may be compiled as the localization and the estimation of a signal with a known form, $u(\tau)$, embedded in noise. When the noise affecting the measurement does not present a particular structure, i.e. when it is white at the scale of analysis, the filtering solution leading to an optimal SNR of the range position of the target is given by the filter adapted to the waveform used, $g_r(\tau) = u^*(-\tau)$.

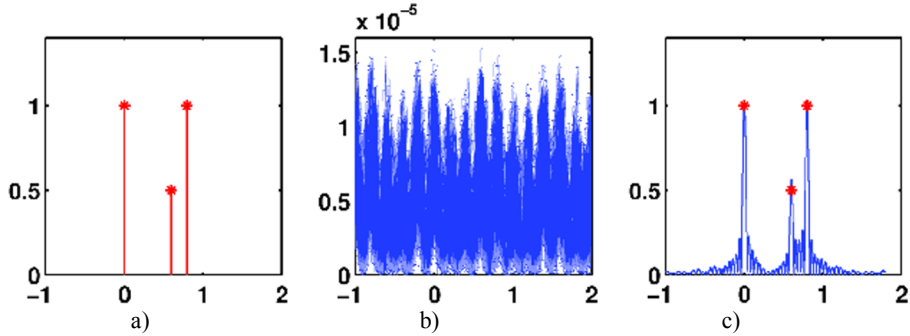

Figure 1.10. *An illustration of the focusing principle in arbitrary coordinates. a) The discrete reflective density $a_c(\tau)$; b) real part of the received signal, made of partially overlapping responses, for large T_{values}, and in the presence of noise; c) reconstruction by focusing the noisy signal received*

The expression of the range focused signal is given by:

$$s_{rf}(\tau) = s_r(\tau) * u^*(-\tau) = \int_{-\infty}^{-\infty} s_r(\tau')\, u^*(\tau' - \tau)\, d\tau' = \sum_{i=1}^{N_s} a_{c_i} h(\tau - \tau_i)\, e^{-j\omega_c \tau_i} + n_f(\tau) \quad [1.14]$$

where $n_f(\tau)$ represents the filtered noise. The function $h(\tau) = u(\tau) * u^*(-\tau)$, which is called the radar impulse response or the range ambiguity function, is maximum at $\tau = 0$ and defines the properties of the focused signal. A simple physical interpretation of range focusing, illustrating the description given by Figure 1.10, may be given using [1.13] and [1.14] and the spectrum of useful signal before and after focusing by adapted filtering [SOU 99], expressed as:

$$S_{r_u}(f) = U(f) \sum_{i=1}^{N_s} \tilde{a}_{c_i}\, e^{-j2\pi f \tau_i}$$

$$\text{and } S_{rf_u}(f) = S_{r_u}(f)\, U^*(f) = H(f) \sum_{i=1}^{N_s} \tilde{a}_{c_i}\, e^{-j2\pi f \tau_i} \quad [1.15]$$

with $\tilde{a}_{c_i} \triangleq a_{c_i} e^{-j2\pi f_c \tau_i}$ and $H(f) = |U(f)|^2$, the Fourier transform of $h(\tau)$. In the frequently encountered case of signal having a flat spectrum and a band width B_f, the reconstruction of measured reflectivity density by adapted filtering is given by:

$$U(f) = \text{rect}\left(\frac{f}{B_f}\right) e^{-j\varphi(f)} \Rightarrow s_{rf_u}(\tau) = \sum_{i=1}^{N_s} \tilde{a}_{c_i} h(\tau - \tau_i) = \sum_{i=1}^{N_s} \tilde{a}_{c_i} B_f\, \text{sinc}(B_f(\tau - \tau_i)) \quad [1.16]$$

with $sinc(x) \triangleq \frac{sin(\pi x)}{\pi x}$ and $\varphi(f)$, an arbitrary phase law. It turns out from [1.16] that as $B_f \to +\infty$, $h(\tau) \to B_f \delta(\tau)$ and the focused signal perfectly reconstructs the equivalent reflectivity density, $s_{rf_u}(\tau) \propto \tilde{a}_c(\tau)$. For a finite band width, the reconstruction is approximated using the function $h(\tau)$ whose concentration improves as the band width becomes larger.

1.2.2.2.2. Focused signal properties

The expressions of the radar impulse response for the different types of presented waveforms are [FER 14]:

$$\mathrm{h_p}(\tau) = \mathrm{T_p}\, tri\left(\frac{\tau}{2\,\mathrm{T_p}}\right)$$

$$h_c(\tau) \approx T_p \, sinc(B_f \tau)$$

$$h_{FMCW}(\tau) \approx h_{SFCW}(\tau) = \frac{sin(\pi N_f \, df \, \tau)}{sin(\pi \, df \, \tau)} \qquad [1.17]$$

with $tri(x)$, the triangular function with unitary amplitude and width and $\Delta f = N_f \, df$ in the case of CW signals. Focusing by adapted filtering can be implemented in the time domain as shown by [1.14] or in the spectral domain. In the case of CW signals, focusing consists of a simple Fourier transform of the received signal demodulated by the emitting signal [FER 14]. The synopsis of a CW radar is given in Figure 1.11 and shows that the recorded demodulated signal corresponds to the spectrum of the ranged focused response, $S_{rf}(f)$.

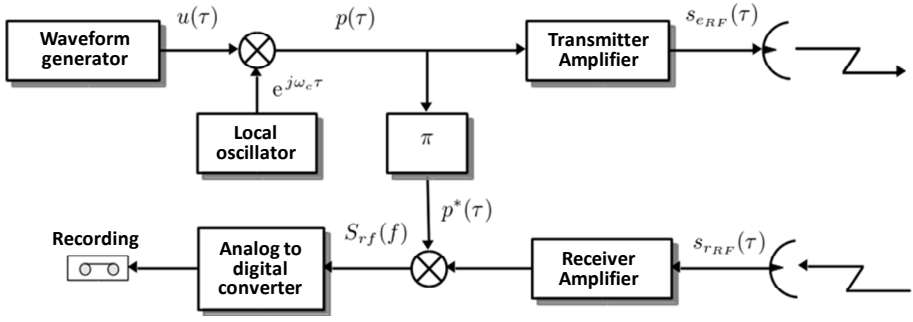

Figure 1.11. *Synopsis of a CW radar*

In Figure 1.12, we can note that if $h_p(\tau)$ and $h_c(\tau)$ have the same temporal support, T_p, the use of a chirp generally leads to a more narrow impulse response. The resolution is generally defined as the minimal distance separating two target coordinates, so that the value of their reflectivity can be estimated without error in the absence of noise, i.e. at the first passage of $h(\tau)$ by 0. The gain in resolution provided by the use of a chirp type waveform can be appreciated in Figure 1.12.

As is shown in Figures 1.10 and 1.13, the use of an adapted filter singularly improves the SNR and allows us to extract the useful signal that was originally embedded in noise. The focused CW waveforms have similar features to $h_c(\tau)$ around $\tau = 0$ and have a similar temporal resolution, $\delta\tau = \frac{1}{B_f}$, that also corresponds to the width of the main lobe of $h_c(\tau)$ at $-3 \, dB$. However, we can note that the CW impulsion responses present a

periodic character with $|h_{CW}(\tau + \tau_{amb})| = |h_{CW}(\tau)| \; \forall \tau$ and $\tau_{amb} = \frac{1}{d_f}$. This property, generated from the definition of the CW signal in the spectral domain, implies that only scenes whose spatial spread verify $\Delta d < \frac{c\,\tau_{amb}}{2}$ can be imaged without ambiguity, in other words without cyclic folding with period d_{amb} after focusing. The summary of the characteristics and limitations for each waveform for range focusing of applications, given in Table 1.1, indicates that the simple pulse does not perform as well as the other waveforms, because the joint improvement of the resolution and the SNR, for a constant emitted power P_e, leads to contradictory constraints concerning the duration of the pulse T_p. In addition, the use of a small value for T_p and a strong amplification at emission require complex electrical solutions that can be avoided using a chirp. The choice of a waveform amongst the three recurring possibilities presented here depends on the available material and on the type of scene observed.

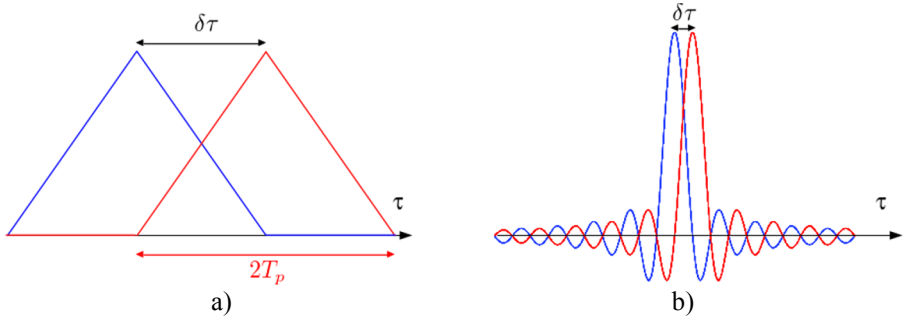

Figure 1.12. *Comparison of the resolution properties of waveforms, of a) simple pulse type and b) chirp*

	Simple impulsion	Chirp	SFCW	FMCW
Resolution δd	$\frac{cT_p}{2}$	$\frac{c}{2B_f} = \frac{c}{2\alpha T_p}$	$\frac{c}{2B_f} = \frac{c}{2N_f d_f}$	$\frac{c}{2B_f} = \frac{c}{2\alpha T_r}$
Sampling	$f_s \geq \frac{1}{T_p}$	$f_s \geq B_f$	$N_f \geq \frac{\Delta d}{\delta d}$	$f_s \geq \frac{\Delta d}{T_r \delta d}$
Gain in SNR	$N_s = \lfloor f_s T_p \rfloor$	$N_s = \lfloor f_s T_p \rfloor$	N_f	$N_f = \lfloor f_s T_r \rfloor$

Table 1.1. *Characteristics of focusing through adapted filtering for different waveforms. N_s and N_f respectively represent the number of values obtained by sampling of a signal in the time domain or spectral range, and $\lfloor x \rfloor$ is the lower/smallest integer value of x*

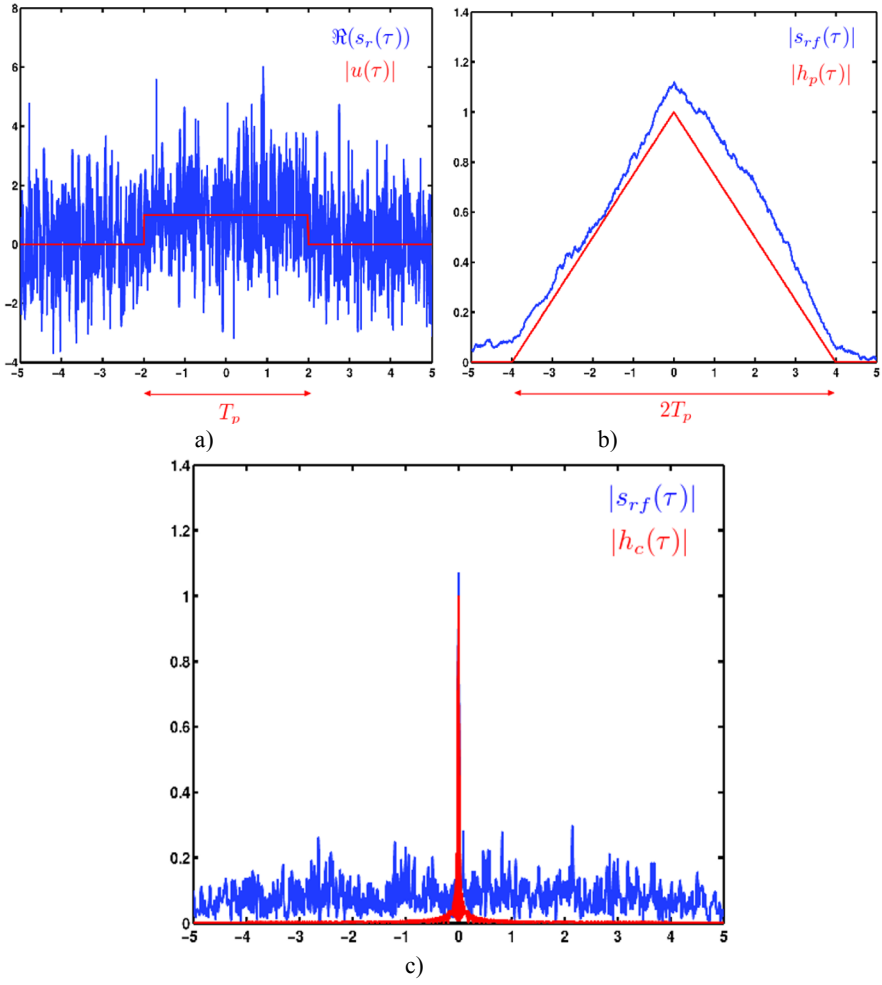

Figure 1.13. *Illustration of the SNR gain provided by adapted filtering. a) The signal received with and without noise. Focused signal in the case of b) a simple impulsion; c) a chirp*

The focused signal is generally represented as a function of the spatial coordinate $d = \frac{c\tau}{2}$ and the wave number, defined from the equivalence $e^{j\omega\tau} = e^{jkd}$, with $k = \frac{4\pi}{\lambda}$, and λ the wavelength. The expression of the wave number shows a factor of 2 compared with common conventions.

The expression of a focused signal for a distributed scene, made up of a large number of non-separable scatterers, is given by $s_{rf}(d) = \int_{-\infty}^{-\infty} a_c(d')\, h(d - d')\, e^{-jk_c d'}\, dd' + n_f(d)$, where $a_c(d)$ represents the scene's equivalent reflectivity density, which for discrete targets, is expressed as $a_c(d) = \sum_{i=1}^{N_s} a_{c_i} \delta(d - d_i)$ and where $h(d) = h(\tau)|_{\tau=2d/c}$. The resolution of a radar measurement strongly influences the estimation possibilities of a scene's characteristics. As is shown in Figure 1.14, the secondary lobes of the impulse response $h(d)$, which are a natural consequence of using band-limited waveforms, can lead to interferences between the different focused responses of the target, which are however separated by distances greater than the resolution. To reduce this effect and to estimate with accuracy the targets' reflectivity we can resort, in practice, to signal processing techniques consisting of implementing a simple spectral weighting (such as the Hamming, Kaiser, etc. techniques), allowing us to significantly lower the level of the secondary lobes at the expense of resolution, or more or less advanced spectral estimation techniques (Capon, MUSIC, etc.) [DEG 98].

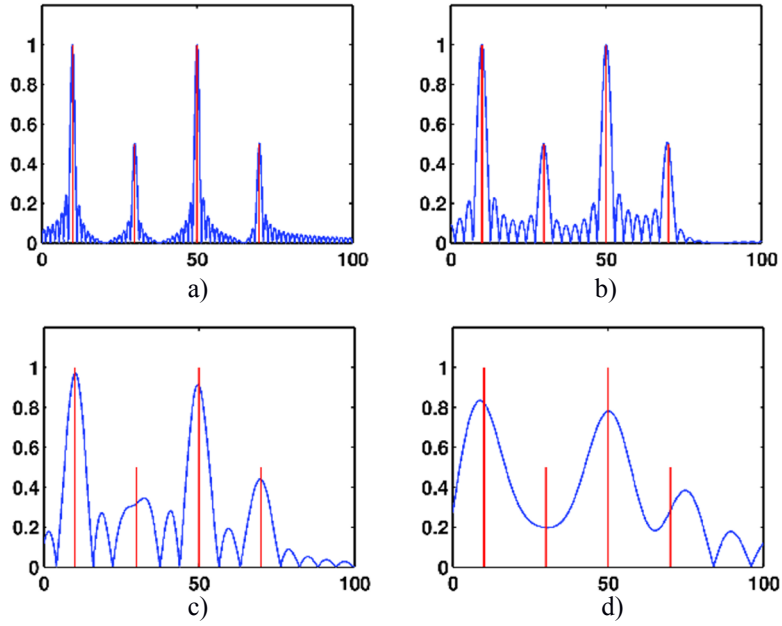

Figure 1.14. *Examples of range focused signals $|s_{rf}(d)|$, with d in arbitrary coordinates, and for targets located at $d_i = \{10,30,50,70\}$, for a spatial resolution $\delta d = 1.42\, n$ with a) $n = 1$, b) $n = 2$, c) $n = 4$, d) $n = 8$*

1.2.3. *2D imaging by synthetic aperture*

1.2.3.1. *Geometric configuration of a SAR measurement*

Here, we consider an airborne or a satellite measurement aiming to map an extended environment that may include artificial or point-like objects. Due to its capacity to differentiate between scatterers according to their radial position, d, an on-board radar at high altitude can be used according to the two principal modes that are illustrated in Figure 1.15. In an altimeter configuration, the radar executes a measurement in the vertical direction that allows us to estimate the vertical distribution of the observed environment and its average elevation with precision, which is dependent on the resolution of the system δd. For mapping applications, the radar is in a side-looking configuration, that allows it to overcome ambiguities in the $\hat{y}$ direction in Figure 1.15 and to naturally better separate the different imaged regions by range focusing, with a ground resolution, $\delta y \approx \frac{\delta d}{\sin\theta}$, that is a function of the local incidence angle. A scene with an arbitrary topography does not directly inform us about the elevation of different scatterers for an arbitrarily topographic scene.

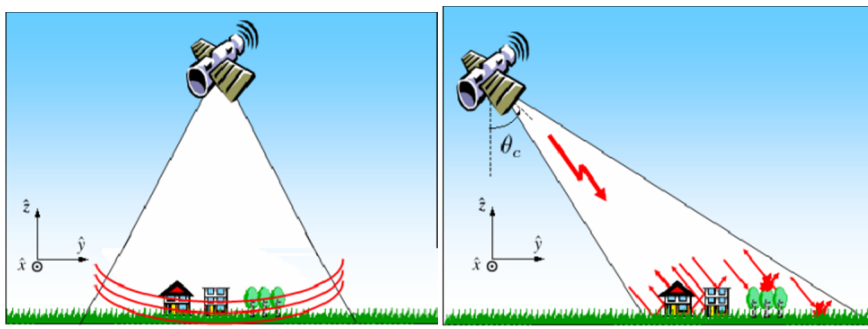

Figure 1.15. *The configuration of a radar measurement: a) by altimetry, b) by a lateral visual*

The antenna system used at the emission and reception of radar signals is an essential part of the SAR measurement. An antenna is characterized by its central working frequency, f_c, its bandwidth, B_f, and its radiation diagram, $G(\theta, \phi)$, which indicates its ability to concentrate used, emitted or received

energy in a given direction of space during the conversion of a signal into a wave. For the sake of simplification, we consider here co-localized transmitting and receiving antennas, having a uniform radiation diagram within an aperture, $(G, \phi) = G\, rect\left(\frac{\phi}{\phi_a}\right) rect\left(\frac{\theta}{\theta_a}\right)$, with ϕ_a and θ_a the antenna apertures in azimuth and elevation, respectively. The characteristics of an antenna, such as the width of its radiation diagram or of its bandwidth, strongly depend on the considered carrier frequency value. To define an order of magnitude of these characteristics, we can use the following approximations [FER 14]:

$$\phi_a \approx \frac{\lambda_c}{L_\phi}, \theta_a \approx \frac{\lambda_c}{L_\theta}, B_f \approx \frac{f_c}{10} \qquad [1.18]$$

with λ_c the wavelength of the carrier signal, L_ϕ and L_θ the antenna's physical dimensions, in m, in the azimuth and elevation directions, respectively. The geometrical configuration of a side-looking measurement is given in Figure 1.16 for a system of antennas aligned with the azimuthal axis, $\hat{x}$. The position of the radar is given by the triplet $(x_a, y_a = 0, z_a = H)$. The position of a point scatterer can be identified by its Cartesian coordinates, (x_0, y_0, z_0), by using the slant range coordinates, (x_0, r_0, z_0), or by using its distance from the radar and angular coordinates, (d_0, θ_0, ϕ_0), with:

$$d_0 = \sqrt{r_0^2 + (x_a - x_0)^2}, r_0 = \sqrt{(H - z_0)^2 + (y_a - y_0)^2}$$

$$cos\, \phi_0 = \frac{H - z_0}{r_0}, tan\, \phi_0 = \frac{x_0 - x_a}{r_0} \qquad [1.19]$$

A scatterer is effectively illuminated by the radar if its coordinates belong to the angular domain covered by the antennas, defined by $|\phi_0| \leq \frac{\phi_a}{2}$ and $|\theta_0 - \theta_c| \leq \frac{\theta_a}{2}$, where θ_c is the central incidence angle for an antenna system.

1.2.3.2. *Limitations of a RAR measurement and principle of azimuth synthetic aperture in azimuth*

Figure 1.17(a) describes a measurement made from a defined azimuthal position $x_a = 0$, of a set of scatterers having azimuthal coordinates verifying $|x_i| < \frac{W_x}{2}$. The range focusing of the received signal allows us to separate certain responses with a resolution $= \frac{c}{2B_f}$, that is however, not sufficient to

differentiate the scatterers P_1 and P_2, i.e. $|d_2 - d_1| < \delta d$. A real aperture radar (RAR) type solution may be imagined using measurements from a single azimuth position and based on the physical characteristics of an antenna system, with the use of an antenna with larger dimensions L_ϕ , with a footprint, W_x, that would be lower than $|x_2 - x_1|$. In the classical situation of a spaceborne sensor, with an altitude $H = 800\,km$, operating with a carrier frequency $f_c = 5\,GHz$, a bandwidth $B_f = f_c/10$, and an antenna system that is characterized by $\theta_c = 25°$ and $\phi_a = 0.2°$, we find $L_\phi = 17\,m$ and $W_x = 3000\,m$. To equal the resolutions in azimuth and in range, that is $W_x = \delta d = 3m$, we should use an antenna with a length $L_\phi = 17.65$ km, which is obviously not a feasible solution in practice! To overcome this significant limitation of the azimuth resolution without modifying the hardware configuration of the radar used, synthetic aperture radar (SAR) measurements, based on azimuth spatial diversity, as illustrated in Figure 1.17(b), may be used

During the radar motion along the $\hat{x}$ axis, the radar-target distances $d_i(x_a)$ follow different paths that can be used to differentiate the two responses (Figure 1.17(c)). Using the expression of the range focused target's response for each measurement position x_a :

$$s_{rf_i}(x_a, d) = a_{c_i}\, h\big(d - d_i(x_a)\big) e^{-j\, k_c d_i(x_a)}\, rect\left(\frac{x_i - x_a}{W_x(r_i)}\right) \qquad [1.20]$$

where $rect\left(\frac{x_i - x_a}{W_x(r_i)}\right)$ signifies that the target belongs to the illuminated zone, we can note that this differentiation can be performed in two ways. First the incoherent information $\left|s_{rf_i}(x_a, d)\right| \propto \left|h\big(d - d_i(x_a)\big)\right|$ may be used which allows us to identify $d_i(x_a)$ with a precision in the order of the range resolution δd. The coherent approach estimates $d_i(x_a)$ through the term $e^{-j\, k_c d_i(x_a)}$, with a precision better than $\frac{\lambda_c}{2} \ll \delta d$. A comparison is shown in Figure 1.18, for a classical radar system, with $f_c = 10B_f$, and shows that when x_a varies on a arbitrarily defined range, $\Delta\, d(x_a) = d_2(x_a) - d_1(x_a)$ remains smaller than δd, making an incoherent differentiation impossible. For the same configuration, $s_{rf_i}(x_a, d(x_a)) = a_{c_i}\, h(0) e^{-j\, k_c d_i(x_a)}$ has a behavior similar to an azimuth chirp whose available positions that allow us to estimate the azimuthal position of the targets. This information can therefore be focused through the means of an adapted azimuthal filter.

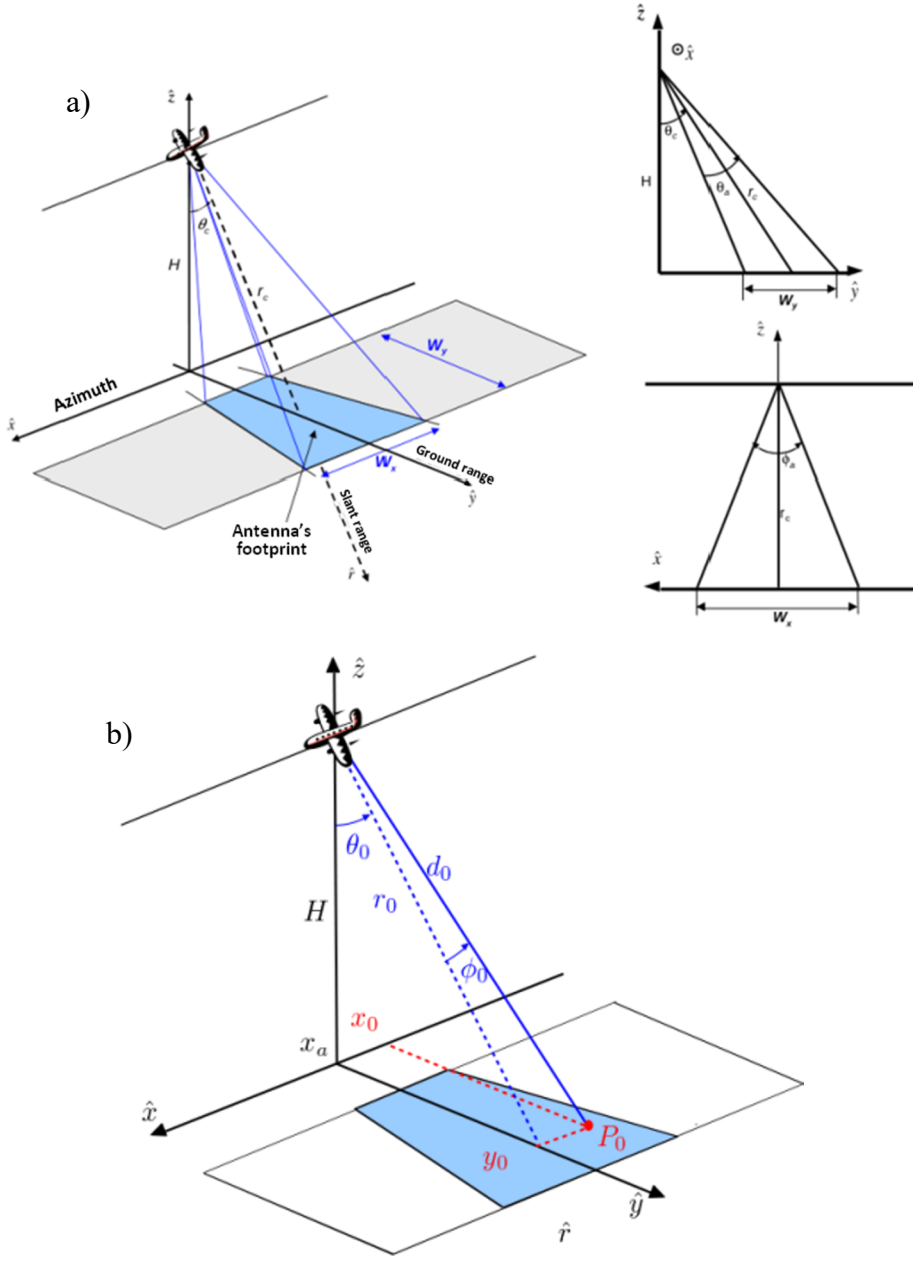

Figure 1.16. *Geometric configuration of an airborne or spaceborne radar measurement: a) illumination characteristics and footprint; b) Cartesian, slant or angular azimuth-range coordinate systems*

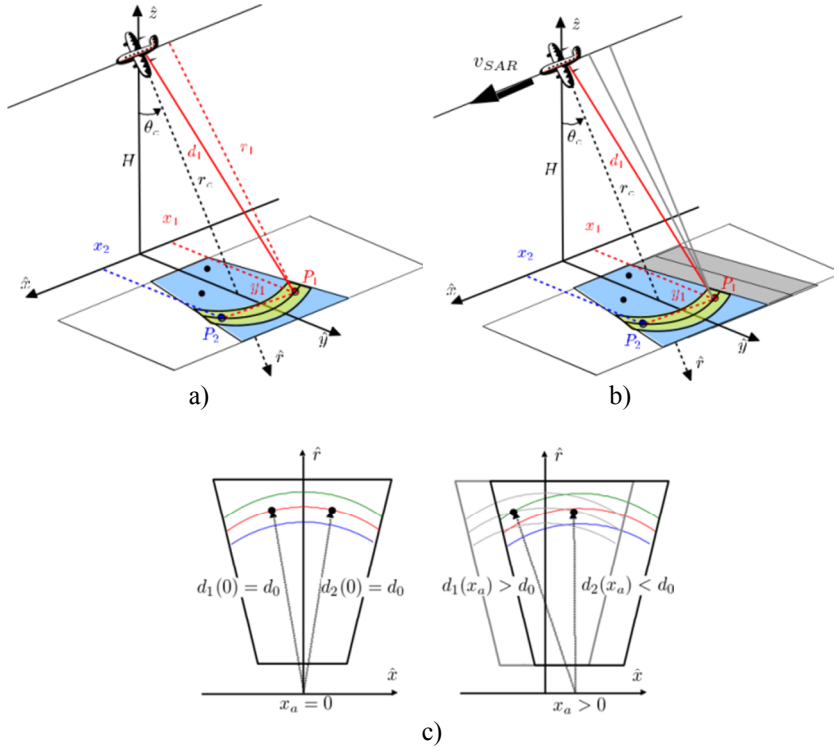

Figure 1.17. *Response of several scatterers of the focusing in range; a) RAR measurement for $x_a = 0$, b) SAR measurement for several values of x_a, c) ambiguous range target differentiation through spatial diversity in azimuth*

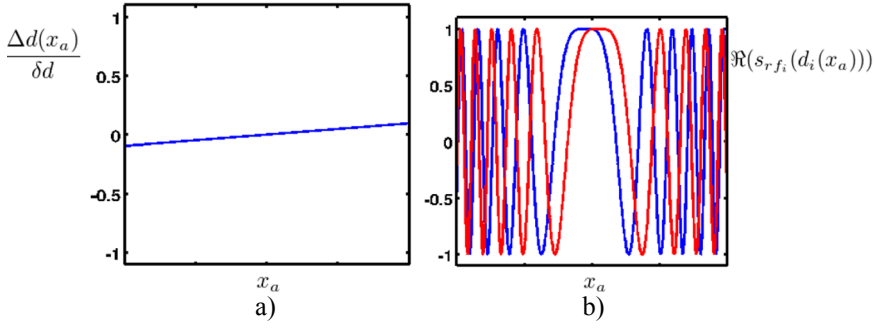

Figure 1.18. *Differentiation of two targets located at $(r_0, \pm x_0)$ by azimuth spatial diversity : a) incoherent, b) coherent*

1.2.3.3. *The SAR focusing by 2D adapted filtering*

In practice, radars are generally mounted on platforms that move in a continuous manner along the azimuth axis, with a speed $\vec{v}_{SAR} = v_{SAR}\hat{x}$, and regularly emit signals with a period $T_r = PRF^{-1}$, where Pulse Repeat Frequency (PRF) is the frequency of emission of the signals in Hz. As is shown in Figure 1.19, this type of measurement is generally considered as equivalent to spatial sampling with a period $dx = \frac{v_{SAR}}{PRF}$, using the stop-go hypothesis, which assumes that the carrier is static during the emission and reception of signals. It may be shown that the effects of motion are generally weak and can be compensated for *a posteriori*. Focusing a measured bi-dimensional signal $s_r(x_a, \tau)$, according to the configuration shown in Figure 1.19, in image $s_{arf}(x, r)$, which is an EM reflectivity image of the observed scene, can be done by means of a 2D adapted filter, constructed using the response of an ideal scatterer that guarantees an optimal statistical character for the imaging operation [LEC 12].

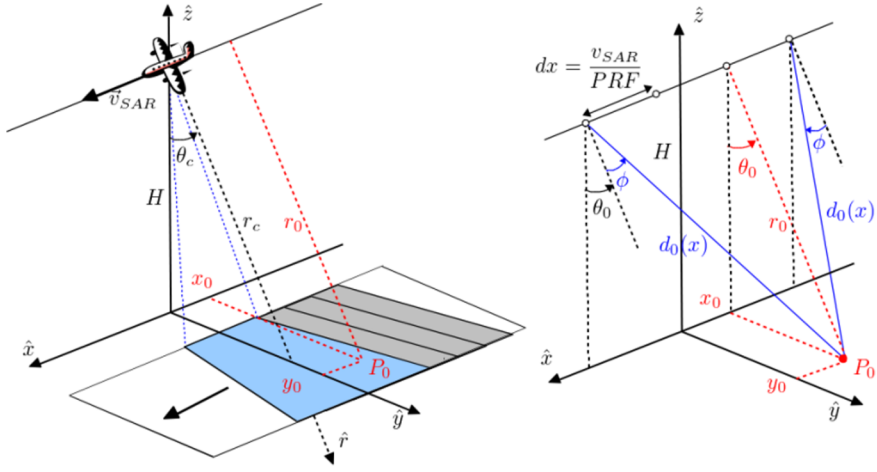

Figure 1.19. *The geometry of a rectilinear SAR measurement with regular sampling*

The 2D SAR response of a scatterer with the coordinates (x_0, r_0) and with an equivalent complex reflectivity a_c is given by:

$$s_r(x_a, \tau) = a_c \, rect\left(\frac{x_0 - x_a}{W_x(r_0)}\right) e^{jk_c d(x_a; x_0, r_0)} u\left(\tau - \frac{2d(x_a; x_0, r_0)}{c}\right) \qquad [1.21]$$

with $\mathrm{d}(\mathrm{x_a};\mathrm{x_0},\mathrm{r_0}) = \sqrt{r_0^2 + (x_0 - x_a)^2}$ and assuming constant propagation losses on the azimuthal aperture, that is $d^2(x_a; x_0, r_0) \approx r_0^2$. This signal can be expressed in the form of a bi-dimensional convolution product according to x and τ, noted $*_{x,\tau}$, as:

$$s_r(x_a,\tau) = a_c\, e^{jk_c r_0}\, \delta(x - x_0)\delta(r - r_0) *_{x,\tau} u_{ar}(x,\tau;r_0) \qquad [1.22]$$

where the 2D convolution core, $u_{ar}(x,\tau;r_0)$, represents the ideal response of a scatterer and may be expressed as [FER 14]:

$$u_{ar}(x,\tau;r_0) = rect\left(\frac{x}{W_x(r_0)}\right) e^{jk_c\tilde{d}(x;r_0)} u(\tau) \qquad [1.23]$$

where $\tilde{d}(\mathrm{x};\mathrm{r_0}) = \mathrm{d}(\mathrm{x_a};0,\mathrm{r_0}) - r_0$ represents the part of the radar-target distance that varies during the radar movement along the azimuth axis. The focusing process is performed using an adapted linear filtering of the scatterer's ideal response, and the focused signal at the arbitrary coordinates (x,r) is given by $s_{arf}(x,r) = \mathrm{s_r}(\mathrm{x_a},\tau) *_{x,\tau} \mathrm{u_{ar}^*}(-\mathrm{x},-\tau;\mathrm{r})$. The evaluation of the convolution operation according to τ leads to a simple expression of $s_{arf}(x,r)$ that uses $s_{rf}(x_a,d)$, the range focused signal:

$$s_{arf}(x,r) = e^{-jk_c r} \int_{-\infty}^{+\infty} s_{rf}(x_a, d(x_a;r,x)) e^{jk_c\, d(x_a;x,r)}\, rect\left(\frac{x-x_a}{W_x(r)}\right) dx_a \qquad [1.24]$$

The focusing of a 2D SAR image can be decomposed in two elementary phases:

– range focusing of the measured signal, $s_r\,(x_a,\tau)$, with the help of an adapted filter as shown by [1.14], for each measurement position x_a ;

– compensation, for each measurement position x_a, of the phase due to of the wave's roundtrip from the radar to the focused arbitrary position, (x,r), using $e^{jk_c d(x_a;x,r)}$ and by taking the sum of compensated signals for the whole azimuth aperture.

Despite its simplicity, this expression requires a significant amount of numeric calculations. In fact, the expression [1.21] can not be processed in a rapid manner using a 1-D Fourier transform according to the only azimuthal direction, given the bi-dimensional character of $s_{rf}(x_a, d(x_a; r, x))$ and the dependence of the second variable, $d(x_a; r, x)$, on x_a. This aspect is illustrated in Figure 1.20, which shows the 2D geometrical area covered by the radar-target distance $\mathrm{d}(x_a; x, r)$. The quantity $\mathrm{d}(x_a; x, r) - r$, that represents the variation of the radar-target range when x_a varies, is called Range Cell Migration (RCM). In a general way, range migration can cover the equivalent of several range cell resolutions and has a range curvature that depends on the value of r, which prevents identical processing, of [1.24] for all range coordinates.

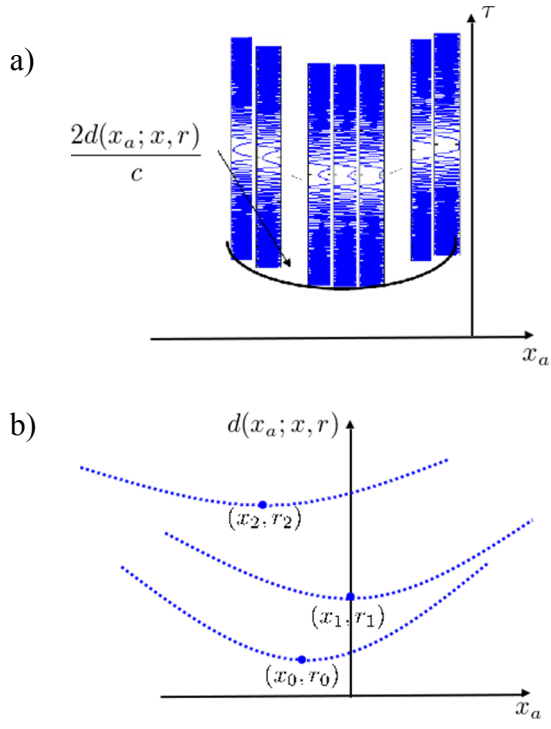

Figure 1.20. *Range migrations a) a measured signal for a single target b) geometric loci described by the radar-target distance, whose curvature varies with r*

In addition, range focusing being generally performed through a fast Fourier transform, FFT, the focused signal is defined at regularly spaced range coordinates at $s_{rf}(x_a, d_{ref} + n\,dd)$, with $n \in \mathbb{Z}$ and $dd \leq \delta d$. The evaluation of [1.24] therefore requires a 1-D interpolation of s_{rf} at irregular coordinates and a numeric sum. The focusing algorithm of the SAR image by 2D adapted filtering is detailed in the synopsis of the Figure 1.21.

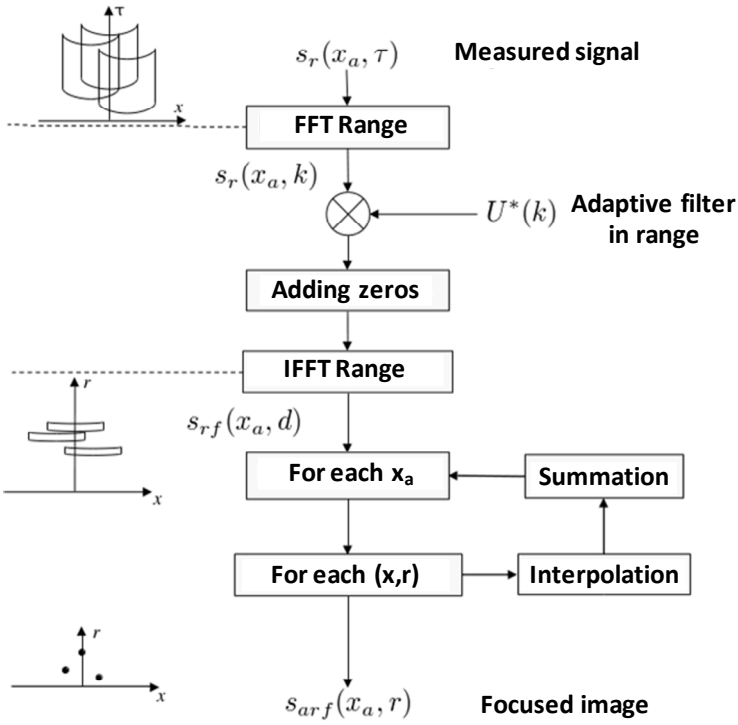

Figure 1.21. *Algorithm synopsis for the SAR focusing using back projection*

The focusing technique presented in [1.24] and described in Figure 1.21 is called back-projection. It operates in the spatial domain and is qualified as "exact", as it does not require any approximation. There are several techniques, exact or approximated, that operate partially or totally on the spectral domain that are less complex. However, we note that back-projection represents an exact and generic solution of focusing, since it can

be adapted to any configurations of acquisition without modification, it has a relatively simple implementation, and its needs in terms of computing power can widely be satisfied with standard calculators.

1.2.3.4. *Azimuth resolution and sampling*

During a SAR measurement, such as that illustrated in Figure 1.19, a scatterer is measured by the radar over a part of the flight path with the length $L_x = W_x$, called the synthetic aperture, defined by the azimuthal angular aperture of the antenna. ϕ_a. Using [1.21], we find that the expression for the range focused 2D SAR response of a target with the coordinates (x, r) presents a constant module and a phase that varies with the radar's azimuthal position, over a part of the track with length L_x :

$$s_{rf}\big(x_a, d(x_a)\big) = a_c\, h(0) e^{-j\, k_c d(x_a)}\, rect\left(\frac{x-x_a}{W_x(r)}\right)$$
$$\propto e^{j\, \varphi(x_a)}\, rect\left(\frac{x-x_a}{W_x(r)}\right) \qquad [1.25]$$

The azimuthal spectral diversity generated by the change of the focused signal's phase term can be quantified using the instantaneous wave number in azimuth given by:

$$k_x(x_a) = -\, k_c \frac{\partial d(x_a)}{\partial x_a} = k_c \frac{x-x_a}{d(x_a)} = \; k_c \sin\phi(x_a), \text{ for } |\phi(x_a)| \leq \frac{\phi_a}{2} \qquad [1.26]$$

The signal thus has an azimuthal spectrum with a constant amplitude over a centered range and with a width $\Delta k_x = 2\, k_c \sin\left(\frac{\phi_a}{2}\right)$. Conforming to what is shown by [1.16], focusing this signal by adapted filtering leads to an azimuth ambiguity function, $h_x(x)$ and a resolution δx, given by:

$$h_x(x) \approx L_x\, sinc\left(\frac{x\, \Delta k_x}{2\pi}\right) \text{ and } \delta x = \frac{2\pi}{\Delta k_x} = \frac{\lambda_c}{4 \sin\left(\frac{\phi_a}{2}\right)} \qquad [1.27]$$

Here, we can see the paradox of the synthetic aperture imagining: the more the radar is originally "myopic", that is ϕ_a and W_x are large, the better its resolution after adapted coherent processing. The azimuth resolution can be related to the physical length of the used antenna, L_ϕ, or to the length of the synthetic aperture in the center of scene, L_x, as:

$$\delta x \approx \frac{L_\phi}{2} \text{ and } \delta x \approx \frac{\lambda_c\, r_0}{2\, L_x} \qquad [1.28]$$

If we re-examine the example of the previously mentioned spaceborne sensor, we find an azimuthal resolution of $\delta x = 8.6\,m \approx \frac{L_\phi}{2}$, much better than the original 3,000 m, and a synthetic aperture length of $L_x = 3{,}081\,m$. During a SAR measurement, a radar regularly emits and receives signals, with a period $T_r = PRF^{-1}$. For a motion with a constant speed v_{SAR}, this leads to a sampling, considered stationary according to the aforementioned *stop-and-go* hypothesis, of the synthetic aperture L_x with a spatial period $dx = \frac{v_{SAR}}{PRF}$, that, in order to avoid all spectral ambiguities must prove $dx \leq \delta x$. The *stop-and-go* hypothesis considers the radar as static during the emitting and receiving of the pulses. As shown in [FER 14], this non-relative approximation generally leads to negligible errors that can be easily corrected *a posteriori*. The PRF value is constrained by the time taken by the signal to travel from the radar to the target and back, which can be represented by a time spread of the scene's range response. The azimuth sampling's frequency is thus subject to the following constraints:

$$4\,sin\left(\frac{\phi_a}{2}\right)\frac{v_{SAR}}{\lambda_c} \leq PRF \leq \frac{c}{2\Delta d} \quad \text{with } \Delta d \approx \Delta r \approx \frac{W_y}{sin\,\theta_c} \qquad [1.29]$$

The generic expression of an environment whose reflectivity density is given by $a_c(x,r)$ is expressed as:

$$s_{arf}(x,r) = \int_{-\infty}^{+\infty}\int_{-\infty}^{+\infty} a_c(x',r')\,e^{-jk_c r'}\,h_{ar}(x-x',r-r')\,dx'dr' \qquad [1.30]$$

where $h_{ar}(x,r) \approx h_x(x)h_r(r)$ is the 2D SAR impulse response. The SNR gain provided by azimuth focusing is given by the number of processed pulses during a measurement, $N_p = \frac{W_x}{dx}$.

When analyzing the gain in SNR provided by 2D focusing using an analytical filter, we can consider separately the case of a point-like scatterer, whose size is smaller than a resolution cell and whose original SNR is given by [1.10], and distributed environments whose SNR before focusing is expressed in [1.11]. In fact, in the case of a distributed environment, the focused reflectivity results from an integration limited to the area covered by a resolution cell and not by the footprint of the antenna system, marked as A

in [1.12]. Thus, the SNR after bi-dimensional focusing can be expressed as [MAS 08]:

$$SNR_{2D_p} = N_r N_p SNR_{raw_p}$$
$$SNR_{2D_e} = N_r N_p SNR_{raw_e} \frac{\delta_r \delta_x}{W_r W_x} \approx SNR_{raw_e} \quad [1.31]$$

where the raw indexes and the 2D respectively differentiate the calculated SNR before or after focusing, p indicates a point target, e an extended environment, and with $N_r = N_f \; or \; N_s$ according to the radar waveform. The gain in SNR, that in practice can attain several dozens of dB for a point-like target, remains close to 1 for extended environments, which is 0 dB.

The quality of a system is generally measured with the help of σ^0_{NE}, the equivalent noise RCS, defined as the minimal RCS for a vast medium with a response that emerges from noise, that is for which $SNR_{2D_e} = 0 \; dB$.

The different steps of the 2D focusing simulated or measured signal are illustrated in Figure 1.22.

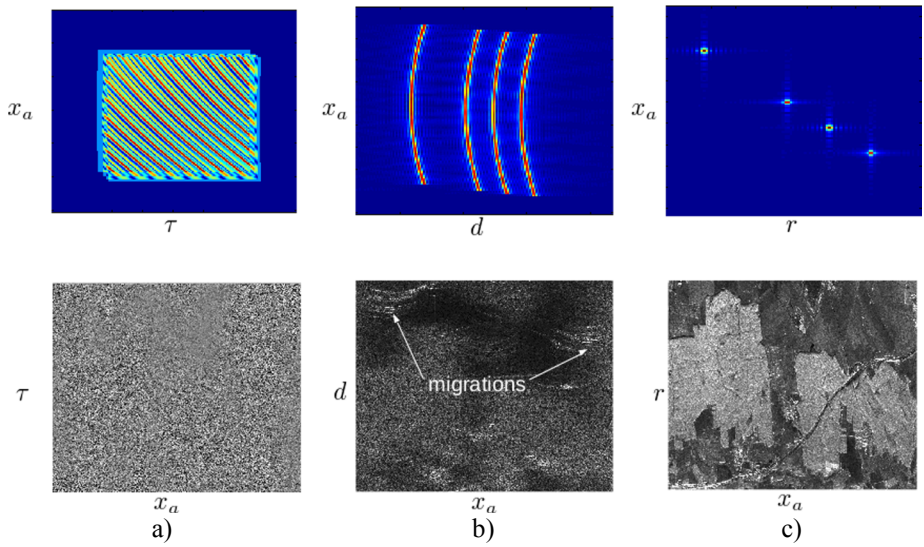

Figure 1.22. *Illustration of the different stages of SAR focusing of simulated signals (above) and those measured by the ESAR sensor from the DLR in the L-band (below): a) measured signal, b) after range focusing, c) after 2D focusing*

Further information concerning the different 2D SAR focusing techniques can be found in the following references: [CAR 95, CUM 05, CUR 91, DEG 98, FER 14, MAS 08, OLI 04, SOU 94, SOU 99].

1.3. Characteristics of SAR images

1.3.1. *Radiometry*

1.3.1.1. *Radiometric content of SAR images*

The characteristics of the interaction between an EM wave and an object or environment strongly depend on the carrier frequency, f_c, the ratio between the wavelength λ_c and the target dimensions defining the analysis scale of the interaction, as well as the preponderance of certain physical phenomena. The carrier frequency defines the central abscissa of the spectral range used during the measurement. Its value determines technological choices for the achievement of a radar as well as the type of possible applications. As is shown in Figure 1.23, the carrier frequency values, generally used for imaging, cover a very wide range, going from VHF and P-band up to W-band.

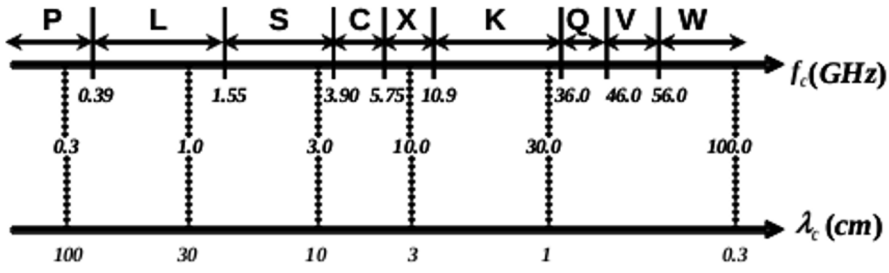

Figure 1.23. *Frequency bands generally used for radar imaging*

The EM scattering properties of a particle, or an object, depend on the ratio between their size and the wavelength. Thus, an irregular natural soil can appear smooth in P-band, with a dominant specular scattering, and very rough in X-band with an isotropic scattering characteristic, as is shown in Figure 1.24.

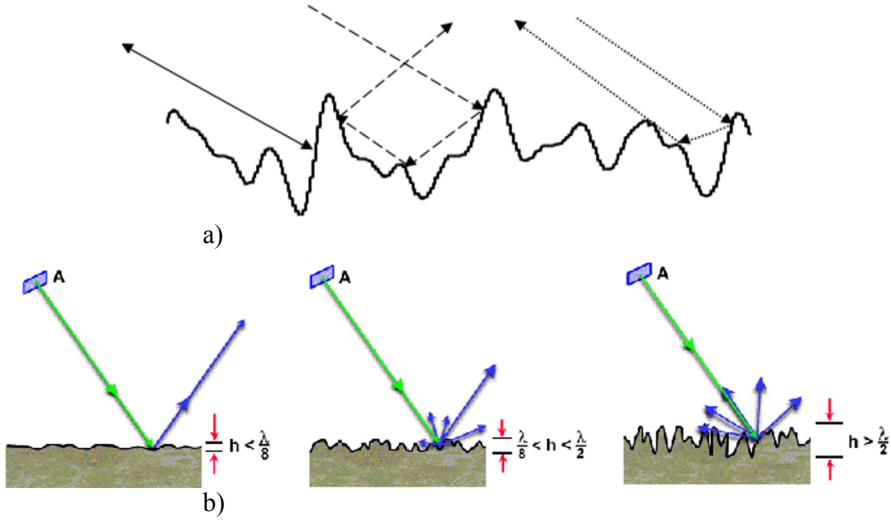

Figure 1.24. *The scattering over rough soil: a) scattering mechanisms, b) influence of the relative size of irregularities*

High wavelengths allow the emitted waves to penetrate volumes. However, for smaller wavelengths, the interactions between waves and volumes' particles represent the dominant scattering mechanism and are characterized by a strong extinction, due to an absorption phenomenon or by scattering in directions other than the considered one. This phenomenon is illustrated in Figure 1.25, which shows three images acquired simultaneously over a tropical forest in X-, C- and L-bands, in the presence of a cloud containing hydrometeors. The cloud appears opaque in the X-band and remains invisible in the L-band. In addition, we note that the texture of the images strongly varies from one image to another, with dark zones, corresponding to smooth surfaces in the L-band, that have a reflectivity comparable to the forest in the X-band.

The images of Figure 1.26 allow us to fully appreciate the complementary properties of radar and optical measurements. It is easier to differentiate between different types of agricultural crop on an optical image. However, the radar allows us, in the L-band, to distinguish between the imaged buildings and forested areas.

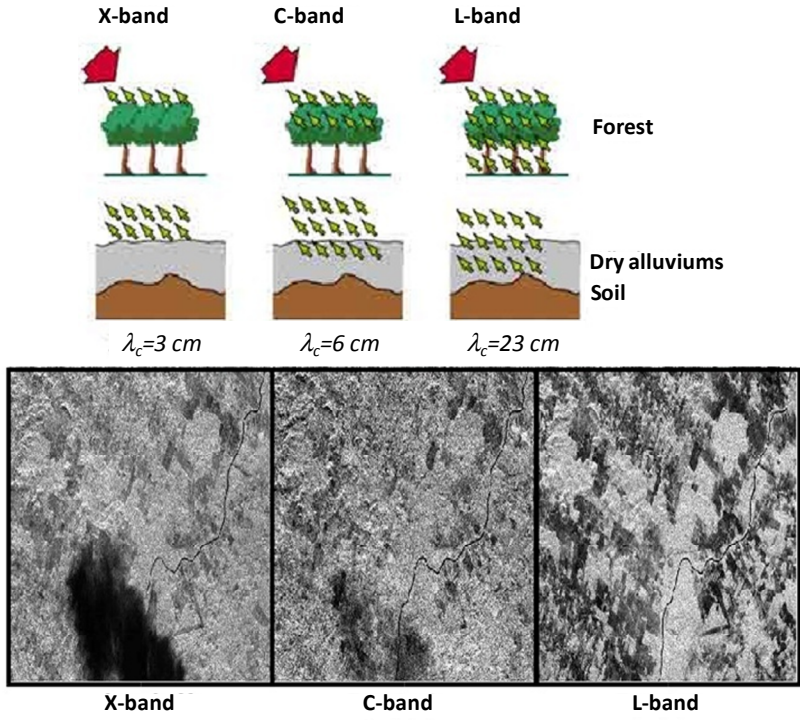

Figure 1.25. *Illustration of penetration the properties over some volumetric environments (above). SIR-C/X SAR images at VV polarization of a tropical forest in the presence of a stormy cloud, simultaneously acquired in the X-, C- and L-bands (below)*

Advanced studies regarding the description, analysis and modeling of interactions between the radar signal and environments, can be found in [ISH 99, TSA 00, TSA 01a, TSA 01b, ULA 81, ULA 82, ULA 86].

1.3.1.2. *Speckle filtering*

1.3.1.2.1. Description of the speckle phenomenon

After range and azimuth focusing, the SAR signal can be expressed, in the absence of a measurement noise, in the simplified form of a 2D convolution given by [1.30] and repeated here, $s_{arf}(x,r) = \int_{-\infty}^{+\infty}\int_{-\infty}^{+\infty} a_c(x',r')\, e^{-jk_c r'} h_{ar}(x-x', r-r')\, dx'dr'$, where $a_c(x',r')$ represents the reflectivity density of the observed scene and $h_{ar}(x-x', r-r')$ is the 2D SAR impulse

response whose width is given by the image's range and azimuth resolutions. The statistical properties of a focused signal may be studied by considering two extreme cases, illustrated in Figure 1.27.

When the resolution cell contains a dominant scatterer at (x_0, r_0), with a reflectivity a_{c_0}, in addition to negligible contributions that form the EM clutter, the reflectivity density is given by $a_c(x,r) = a_{c_0}\,\delta(x - x_0, r - r_0) + \epsilon$, and [1.30] is simplified as $s_{arf}(x,r) \approx a_{c_0} e^{-jk_c r_0} h_{ar}(x - x_0, r - r_0)$. When the resolution cell contains a large number of independent scatterers, uniformly distributed, with random amplitudes and phases, the reflectivity density is a spatially uncorrelated random process, $\left(a_c(x,r)a_c^*(x',r')\right) = \sigma_a(x,r)\,\delta(x - x', r - r')$, with E the mathematical expectations operator, and [1.30] cannot be simplified. The statistical aspect of the SAR response, formed by the sum of contributions within a resolution cell, is illustrated in Figure 1.28. In the case of a preponderant point-like scatterer, the SAR response, dominated by the principal contribution, is nearly deterministic. In the case of numerous and uniformly distributed contributions, the focused signal can be associated with a random movement on the complex plane and $s_{arf}(x,r)$ is a random variable [GOO 76].

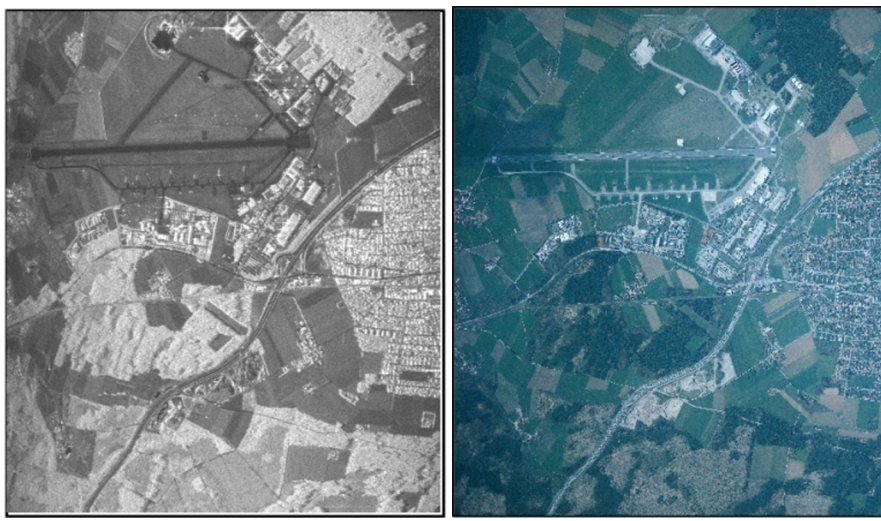

a) b)

Figure 1.26. *a) polarimetric span of a SAR image (total power received over the four channels of a polarimetric radar system) acquired by the sensor, DLR/ESAR in the L-band; b) an optical image*

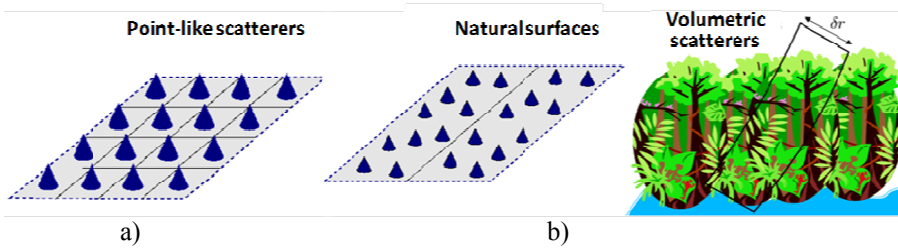

Figure 1.27. *Illustration of the EM reflectivity density within a SAR resolution cell containing a) a dominant scatterer, b) a very large number of distributed scatterers*

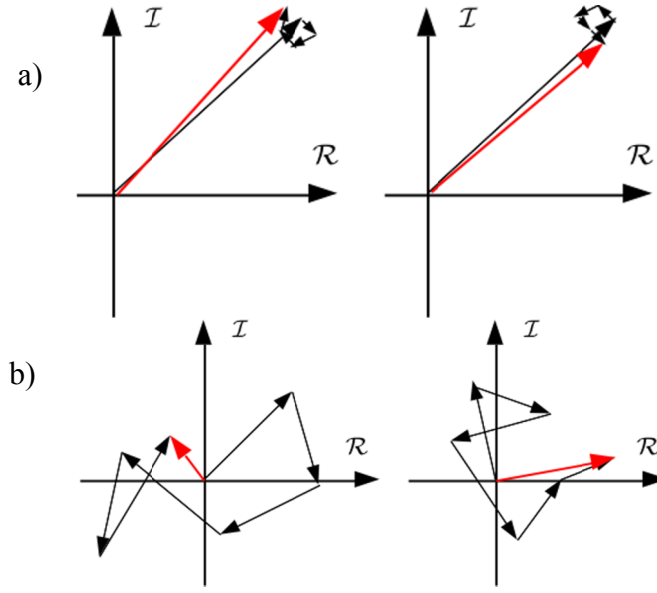

Figure 1.28. *Two realizations of coherent sum within a resolution cell containing: a) a dominant point scatterer, b) distributed scatterers*

Within a homogeneous environment, composed of independent scatterers or a continuous density, the SAR response, $s_{arf}(x,r)$, experiences very strong variations of amplitude from one resolution cell to another, created by small variations in the radiometric or geometric configuration of a large number of measured scatterers. This effect, called speckle, is inherent to the use of a coherent imaging system and should not be qualified as a noise despite its random aspect. For a large number of scatterers within a

resolution cell and by applying the central limit theory, the SAR response is modeled in the form of a product:

$$s_{arf}(x,r) = \sqrt{I(x,r)}\,\eta(x,r)\ ,$$

$$\text{for which we note: } s(l) = \sqrt{I}\,\eta(l) \qquad [1.32]$$

where I is the intensity of the response that can be related to σ, the average reflectivity of the medium. l is the index of a realization of the complex Gaussian random variable, $\eta \in \mathbb{C}$, with zero mean and unitary variance and a uniform phase distribution, composed of independent real and imaginary parts that are centered with a variance of 1/2. The SAR image then follows a complex Gaussian law specified by [GOO 76]:

$$f_s(s) = \frac{1}{\pi I} e^{-\frac{|s|^2}{I}}\ \text{, with } E(s) = 0, var(s) = I$$

$$f_{arg(s)}(\phi) = \frac{1}{2\pi} \text{ and } f_{|s|^2}(\rho^2) = \frac{1}{\pi I} e^{-\frac{\rho^2}{I}} \qquad [1.33]$$

Given its uniform distribution, the s argument is not exploitable *a priori*, whereas $\hat{I} = |s|^2$, the maximum likelihood (ML) of I, gives information concerning the observed environments' reflectivity, with $E(\hat{I}) = I$ and $var(\hat{I}) = I^2$. The standard deviation of the positive magnitude $\hat{I}$ is equal to its average value, which is a consequence of a very large variability and therefore of a very approximative estimation of I through the measurement of $\hat{I}$ [LEE 94]. This characteristic relationship is illustrated using real data from Figure 1.30(b).

1.3.1.2.2. Speckle filtering using incoherent averaging

Several independent outputs, or views, of the measurement $\{s(l)\}_{l=1}^{L}$ are used to improve the quality of the estimation. The distribution of L independent realizations $s(l)$ is given by:

$$f(s(1), \cdots, s(L)) = \prod_{l=1}^{L} f\big(s(l)\big) = \frac{1}{\pi^L I^L} e^{-L\frac{\hat{I}}{I}}$$

with

$$\hat{I} = \frac{1}{L}\sum_{l=1}^{L}|s(l)|^2 \qquad [1.34]$$

where $\hat{I}$, the L-look ML estimate of I, is given by the empirical mean of single intensities and presents a considerably reduced variability for a large number of views, with $E(\hat{I}) = I$ and $var(\hat{I}) = \frac{I^2}{L}$. As is shown in Figure 1.29, the use of L independent looks leads to the concentration of the distribution of $\hat{I}$ around its average value, I, which provides a reflectivity estimate whose reliability improves as L increases. Among the different approaches allowing us to generate L independent samples belonging to the same distribution, the most commonly used is based on the selection of responses. Under the hypothesis of a local stationary reflectivity, that is $I(x,r)$ is constant around (x_0, r_0), this technique allows us to guarantee an optimal character for the given estimate in [1.34] and to better estimate $I(x_0, r_0)$. As shown in Figure 1.30, a speckle filter can be implemented using a sliding window defining a neighborhood for the sampling of L independent outputs. We can note that filtering allows us to better differentiate the scene's different patterns of a scene in a general manner but leads to an alteration of the information over heterogeneous zones, represented here by bright points, as the local stationary hypothesis is not respected. There exist a wide variety of speckle filters, all using different estimation techniques of I [LEE 94, TOU 02].

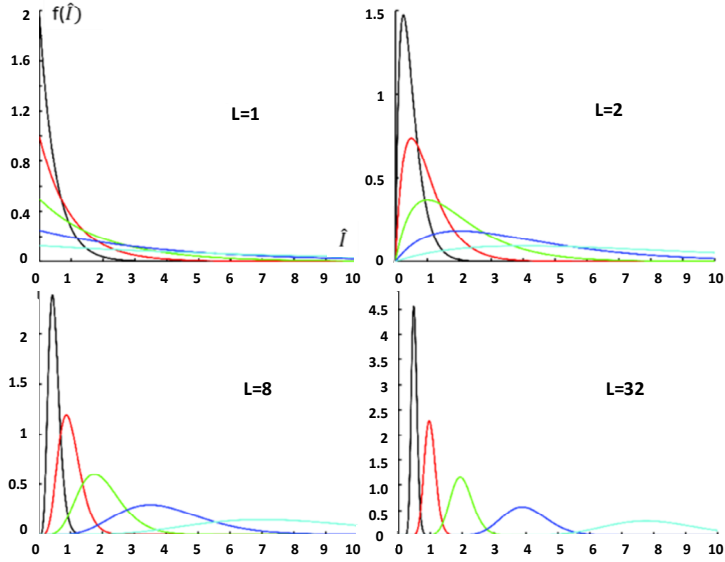

Figure 1.29. *Distribution of Î for I= 0.5 (black), 1 (red), 2 (green), 4 (blue), 8 (cyan) for a different number of looks, L*

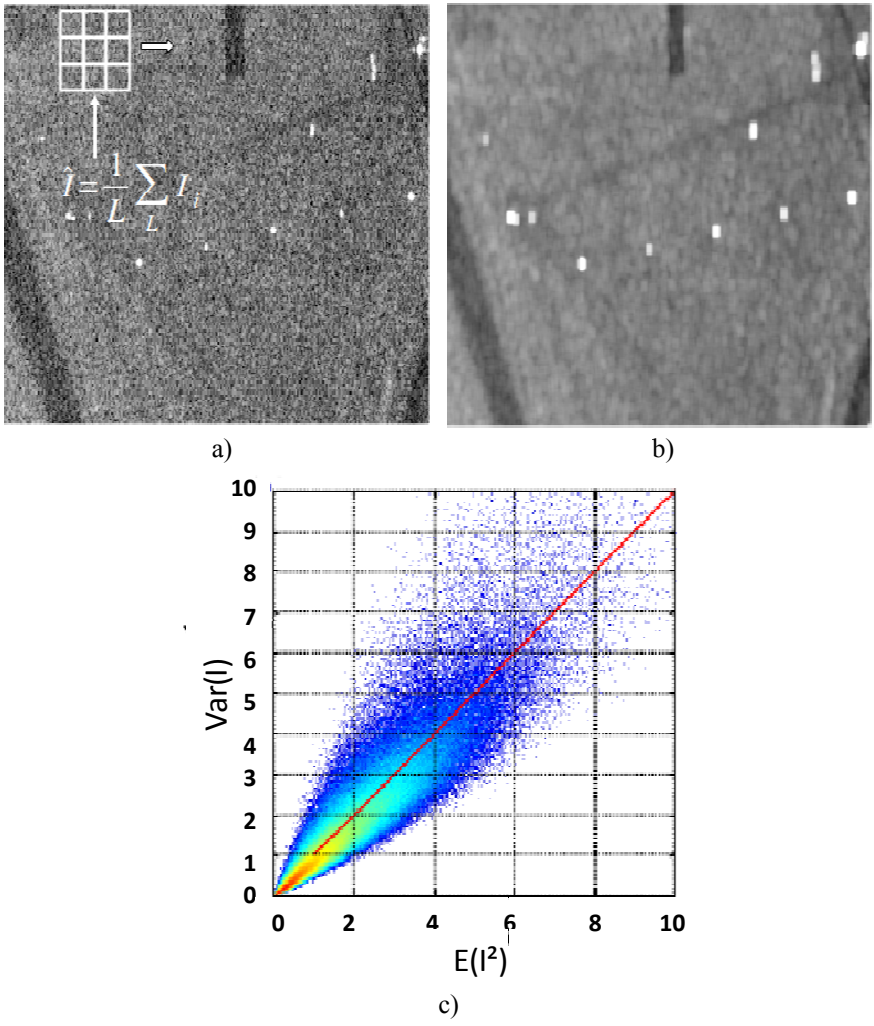

Figure 1.30. *An E-SAR image acquired in the L-band over the DLR site in Munich, Germany: a) single look, b) after (7 × 7) boxcar filtering, c) illustration of the multiplicative nature of the speckle effect*

1.3.1.2.3. Some speckle filtering techniques

The objectives of speckle filtering firstly involve reducing the variance of the intensity, i.e. the spatial fluctuations due to the speckle effect, and

secondly, maintaining the image's texture, i.e. the spatial fluctuations that form the information contained in the SAR image. The filtering quality is generally quantified over *a priori* homogeneous zones having a response that follows a normal law, using the equivalent number of views, N_{eq}, obtained with the variation coefficient, $\varrho(I)$, defined as $\varrho(I) = \frac{std(I)}{E(I)} = \frac{1}{\sqrt{N_{eq}}}$. A quality filter assures a large value of N_{eq}. The evaluation of criteria linked to the respect of the spatial information is more subjective. Thus, we can check that a filter preserves the contours of homogeneous zones, and does not affect the response of the deterministic scatterers.

Estimation Techniques: The major part of the current filtering techniques use an estimation having a form similar to those presented in [1.34], $\hat{I} = \frac{1}{L}\sum_{l=1}^{L} w_i |s(l)|^2$, with $\{w_i\}_{i=1}^{L}$, a set of real weights, with $\sum_{l=1}^{L} w_i = L$. Particular 2D weighting functions, such as a Gaussian, or a Laplace or triangular function, allow us to naturally preserve contours or heterogeneities, at the expense of the filtering's strength which only attains its optimal value over homogeneous zones with a uniform weighting. Here, we can cite the original technique, developed by J.S. Lee, that proposes an adaptive estimation approach, whose form is adapted to local statistics [LEE 94]. The proposed filter combines the single-look intensity, $I_0 = |s(l_0)|^2$, i.e. non-filtered, with the classically filtered term, $\bar{I} = \frac{1}{L}\sum_{l=1}^{L}|s(l)|^2$, using a coefficient that is based on local statistics:

$$\hat{I} = \bar{I} + b(I_0 - \bar{I}) ,$$

with:

$$b = \frac{1-q}{1+p} , q = \frac{1}{\hat{\varrho}^2(I)} , p = N_{eq_0}, 0 \leq b \leq 1 \qquad [1.35]$$

where the variation coefficient $\hat{\varrho}(I)$ is estimated in the neighborhood of the pixel to be filtered and N_{eq_0} represents the signal's number of equivalent views before filtering, $N_{eq_0} = 1$, if $\bar{I}$ is estimated from $|s(l)|^2$. When the evaluated pixel's neighborhood is homogeneous, $b \to 0$, $\hat{I} \to \bar{I}$ and the filter adopts an optimal behavior for a uniform texture. When the environment presents an intensity with a strong variance, $b \gg 0$ and $\hat{I} \to I_0$, the filter only slightly modifies the intensity of the pixel to be filtered. This type of environmental adaptation allows us to avoid an irremediable alteration of the image's texture.

Sample Selection Techniques: The major differences between the fundamental filtering techniques concern the selection, $|s(l)|^2$, taken into account for the estimation of the local statistics of the intensity [TOU 02]. Here, we can cite three alternative approaches to the boxcar, presenting a growing level of complexity. The refined Lee filter [LEE 99] is based on a series of simple masks, illustrated in Figure 1.31, for selecting the part of the window used to estimate $\overline{I}$. The choice of a window amongst the eight that are proposed is based, according to the version of the considered filter, on maximal homogeneity criteria using a variation coefficient, or on intensity gradients aiming to avoid an excessive filtering of small targets. The IDAN filter [VAS 06] proposes another type of neighborhood, defined as the set of the image's pixels forming a set of connected pixels adjacent to the pixel to be filtered and which are likely to belong to the same statistical distribution. This approach allows us to define estimation zones with arbitrary forms that are particularly well adapted to highly textured images, such as urban zones. The test of the statistical homogeneity is evaluated through statistical similarity criteria. The third technique mentioned here is based on a non-local statistical estimation technique [DEL 09]. A patch is defined around the observed pixel, and patches presenting similar patterns are searched for within the whole image. The series of patches resembling the one over the pixel to be filtered is then used to estimate the filtering parameters [DEL 15]. Filtering examples that illustrate these three approaches are given in Figure 1.32. It is important to note that many different filtering techniques exist, and an exhaustive and thorough presentation of all of these would be out of the scope of this chapter.

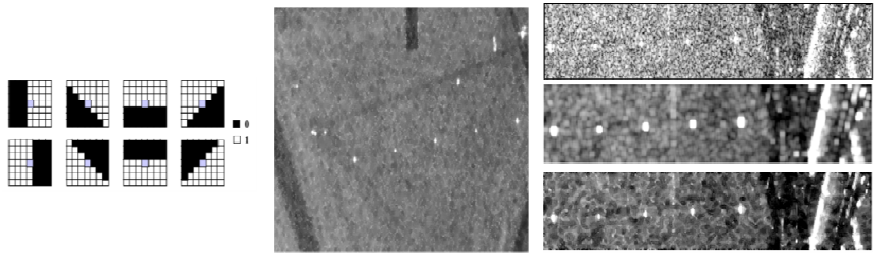

a) b) c)

Figure 1.31. *Illustration of the Lee speckle filter: a) directional masks; b) image from the DLR after (7 × 7) Lee filtering; c) single-look details (above), after boxcar filtering (middle), Lee (below)*

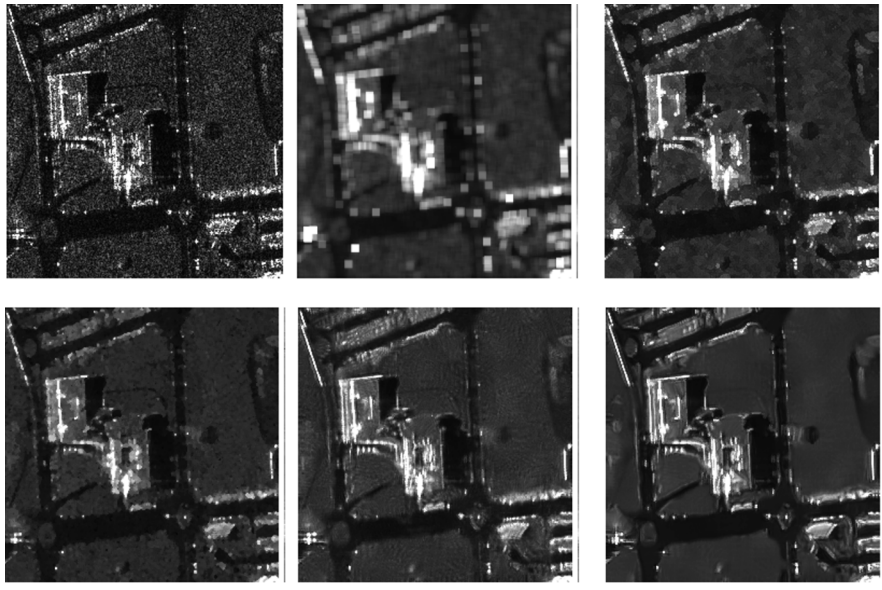

Figure 1.32. *Comparison of speckle filters proposed by [DEL 15] on an ONERA/SETHI image acquired at sub-metric resolution: a) a single-view image and results of filtering; b) boxcar; c) refined Lee; d) IDAN; e) non-local, one iteration; f) non-local with several iterations*

1.3.1.3. *Influence and compensation of a scene's topography*

The topography of a scene is a parameter that must be accounted for when analyzing the SAR response of an environment. In fact, the local incidence angle θ_{loc}, defined as the angle between the radar line of sight and the normal to the local range slope not only influences the value of a medium's EM reflectivity, but also the measurement taken by the SAR. As indicated in Figure 1.33, the local incidence angle can vary in significant proportions as a function of the scene's topography, but also of the radar's trajectory, that defines the value of viewing angle, in range, θ_r. This angle can vary by a few degrees inside a spaceborne image and a couple of dozen degrees for airborne measurements. The reflectivity curves in Figure 1.33 show that the sensitivity of the response of an area to variations of θ_{loc} is strongly dependent on certain physical characteristics, including the roughness: a smooth surface, with high kL_c, L_c being the correlation length of the surface, presents a strong dependency on the angle of measurement, whereas a very

rough surface has a less anisotropic response, leaning towards the response of a volumetric medium. The SAR image of Figure 1.33, is characterized by strong textural information, mainly caused by a modulation by the local topography.

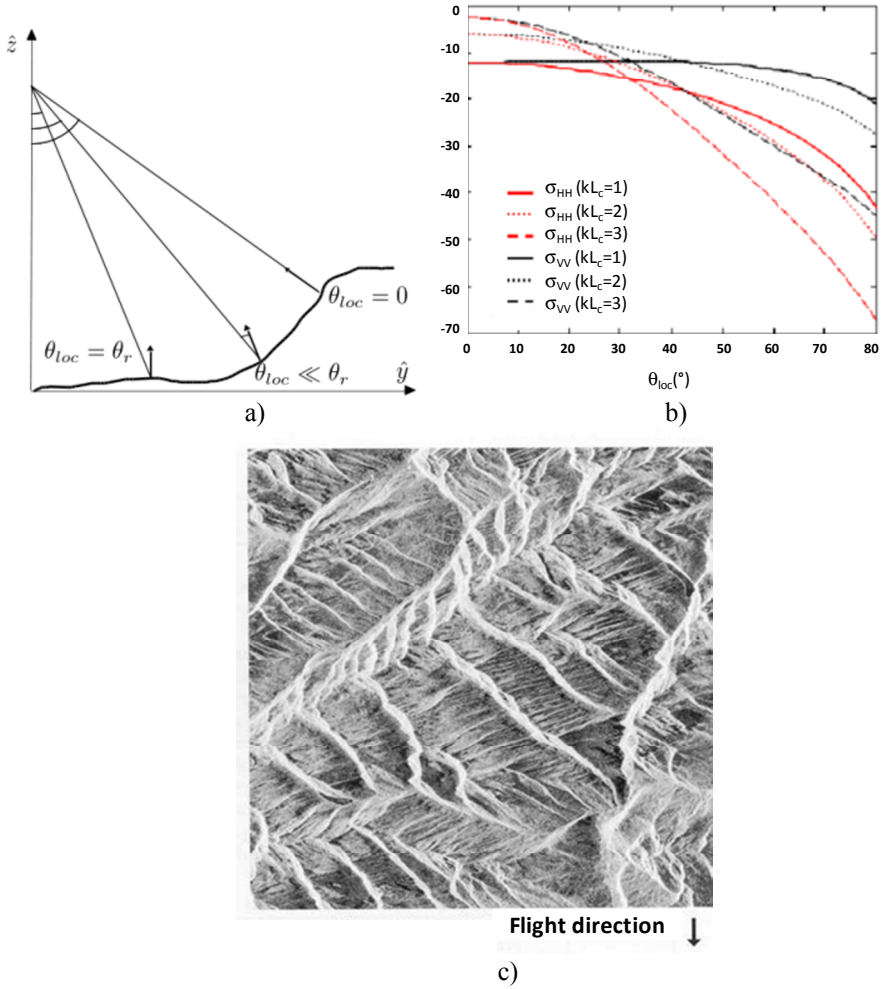

Figure 1.33. *Influence of local topography on a scene's reflectivity: a) variations of θ_{loc} with the topography of a scene; b) surface reflectivity (SPM model [ULA 82]) for different values of roughness; c) ERS-2 images acquired in the C-band (incidence angles 24°–26°)*

The local topography can also imply a modulation of the intensity of a SAR image, made of a set of resolution cells regularly spaced in range, whose geometry does not correspond to that of an arbitrary scene. The SAR intensity is generally modeled as $I(x,r) \propto \frac{P_e G_e G_r \lambda^2 \sigma^0 A}{(4\pi)^3 d^4}$ where P_e, G_e, G_r respectively represent the power emitted power and the antenna gains, the term $\sigma^0 A = \int_{cell} \sigma(x,r)\, dA$ represents the average measured reflectivity within a resolution cell. The illustration in Figure 1.34 shows the different conventions used to compute the surface A, used for the estimation of the local reflectivity density as [SMA 11]:

$$\xi^0(x,r) \propto \frac{I(x,r)}{A_\xi(x,r)}, \text{ with } \xi = \beta, \sigma, \gamma \qquad [1.36]$$

where $I(x,r)$ represents the estimated intensity in the range azimuth domain, and $\beta^0, \sigma^0, \gamma^0$ are the local reflectivity densities in the *slant range*, in ground range, or in the perpendicular plane, all given by the following types of expression [ROS 04]:

$$\beta^0(x,r) = \frac{I(x,r)}{K\, G^2(\theta(x,r))} \left(\frac{r}{r_{ref}}\right)^4$$

$$\sigma^0(x,r) = \beta^0(x,r)\, sin(\theta_{loc}(x,r))$$

$$\gamma^0(x,r) = \frac{\sigma^0(x,r)}{cos(\theta_{loc}(x,r))} \qquad [1.37]$$

where $\theta_{loc}(x,r)$ is the local incidence angle, not represented in Figure 1.34, and K is an absolute calibration constant.

Here, the approach illustrated in Figure 1.33 only corrects the effects linked to regularly spaced meshing and to cylindrical symmetry of a zone of arbitrary topography, through the compensation of the modifications of the area covered by one pixel with a scaling factor applied to the image intensity. This approach is based on the assumption of the type of surface of the imaged medium and on the precise knowledge of the imaged zone's relief.

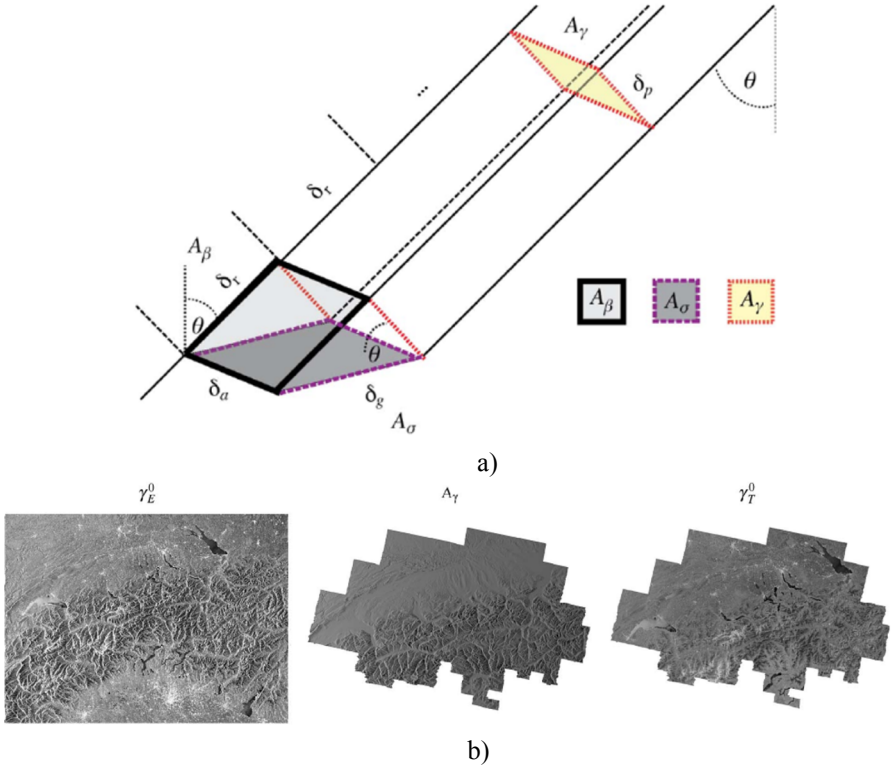

Figure 1.34. *a) Conventions used for calculating the measured intensity's normalized surface; b) example of compensation on an Envisat ASAR WS VV image [SMA 11]; γ_E^0 corresponds to an estimation of θ_{loc} using a reference ellipsoid, whereas γ_T^0 uses a much more precise terrain model, allowing the mapping of local areas $A_\gamma(x,r)$*

1.3.2. *Geometry*

1.3.2.1. *Geometric distortions of a SAR image*

A SAR image is a 2D representation, on the $(\hat{x},\hat{r})$ plane, of the response of a 3D environment, defined in the 3D system $(\hat{x},\hat{y},\hat{z})$. For optical measurements taken in a vertical direction, the reduction in dimensions relates to a simple loss of depth in the $\hat{z}$ direction and gives way to an easy interpretation. For the SAR measurements, the reduction takes the form of a cylindrical projection given by $r = \sqrt{(H-z)^2 + y^2}$, that generates

distortions that must be accounted for when interpreting an image. We can discriminate three significant types of distortion, illustrated in Figure 1.35:

– Foreshortening: the projection of a facet of the imaged surface on the radial axis gives way to foreshortening, that is a function of θ_{loc}, the local incidence angle, given by $\theta_{loc} = \theta - \alpha$, with α, the local slope in range. In an extreme case, when $\alpha = \theta$, the facet is projected on a single point on the radial range axis;

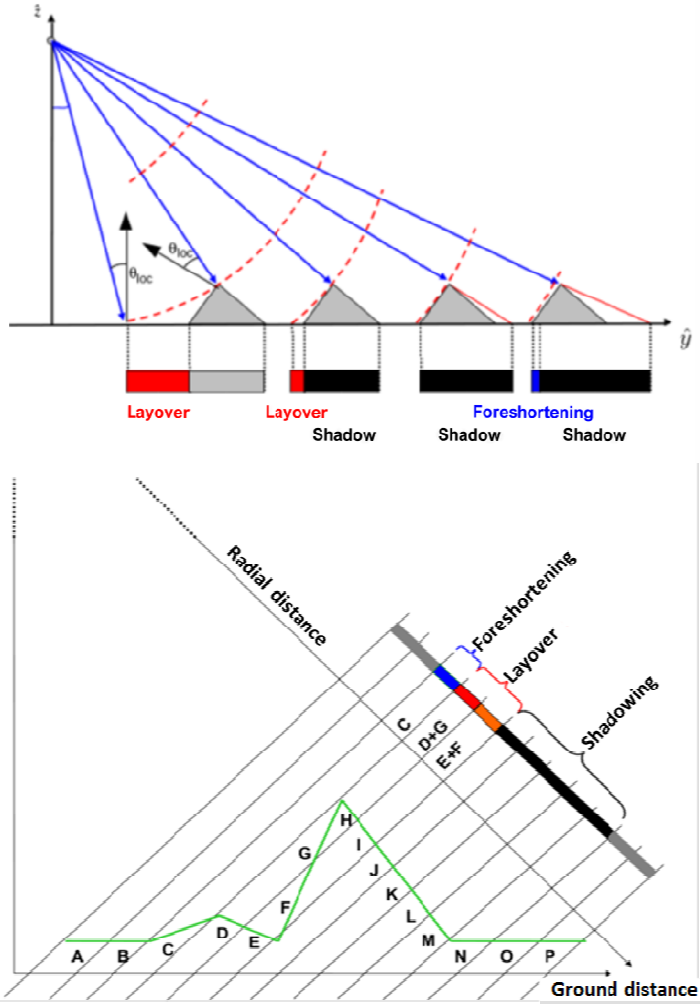

Figure 1.35. *Geometric distortion phenomena for SAR imaging*

– Layover: when $\alpha > \theta$, foreshortening transforms into layover. In this case, the radial distance of the top of a tall structure α is less than that of the base, the top thus appears before the base in a SAR image and the measured object thus lays over in the direction of the radar;

– Shadowing: when $\alpha < -\theta$, the facet at hand is no longer illuminated by the radar, and the corresponding pixels are filled in with noise. In practice, the reflectivity attains a minimum value that is comparable to the noise floor of the radar system, for values of $\theta_{loc} > 80°$. These phenomena are illustrated by the SAR images in Figure 1.36.

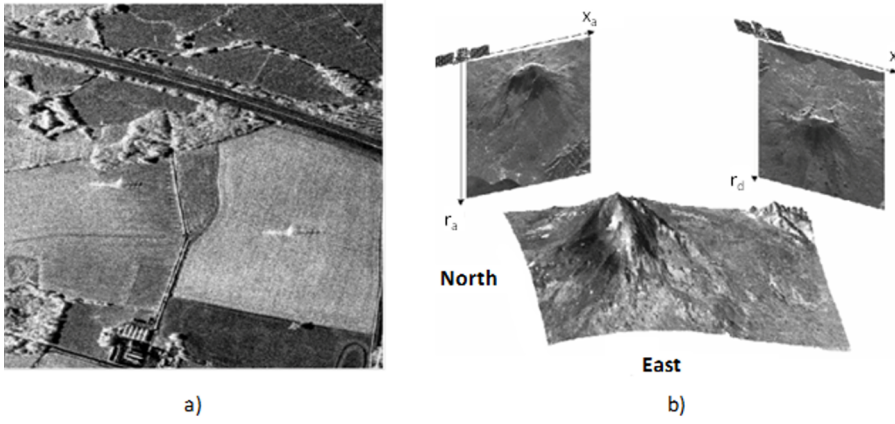

Figure 1.36. *Examples of geometric distortions. a) Electric pylons imaged by the F-SAR sensor of DLR; b) volcano measured over ascending and descending paths of a satellite sensor, image made available by Politecnico di Milano, Italy*

1.3.2.2. *Influence of spatial resolution*

Spatial resolution plays an important role for a certain number of applications, in particular those related to the characterization of complex environments, such as dense urban zones, or to the detection and the recognition of small targets. As is shown in Figure 1.37, low resolution sensors are well adapted to the observation of phenomena at a large scale since they operate in large spatial coverage modes, but such sensors are not adapted to the refined characterization of urban environments that appear as compact zones, with strong reflectivity. This type of image is not well

adapted to small target detection for which the response inside a resolution cell is dominated by the ambient clutter. The improvement in resolution allows us to retrieve a large number of characteristic details of certain types of scattering mechanisms (layover, shadowing) and is generally accompanied by a singular increase of the complexity of the images. Very high resolution data allows us to foresee an important quantity of new applications, such as the characterization of very small vegetal zones in urban environments, and the inspection of structures and buildings that was not possible in the past.

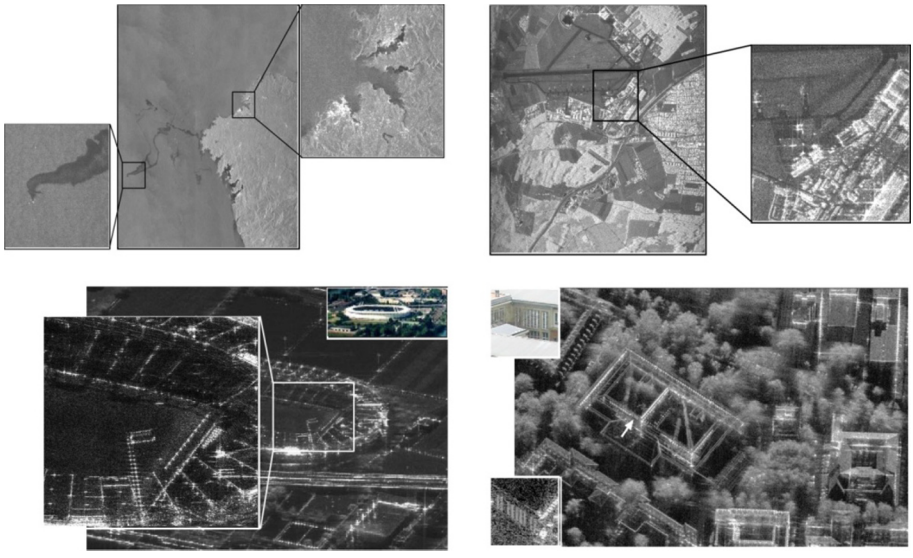

Figure 1.37. *SAR images with different resolutions. ESA/EnviSAT/ASAR image (C-band, 25 m) of the Prestige disaster, off the shores of Galicia, Spain (above left). DLR/E-SAR image (L-band, 2 m) of the DLR, Munich, Germany (above right). CNES-ONERA/Ramses images (X-band, 10 cm) of the Toulouse Stadium (below left). FGAN/Pamir image (X-band, 10 cm) of the Karlsruhe campus, Germany (below right), from [SOR 06], the arrow indicates the position in the image of the two detailed view which are proposed on the left hand side of the image*

1.3.2.3. *Different SAR imaging modes*

The imaging mode previously presented, that is also the most commonly used, is called *Stripmap*. It is characterized by a system of antennas having fixed viewing angles in range θ_c, and in azimuth ϕ_c, and by a rectilinear nominal trajectory. As was presented before, the range resolution is fixed

by the bandwidth, of the effectively emitted signal, and the azimuth resolution is a function of the antenna's azimuthal aperture, ϕ_a, that can be related to the length of the synthetic aperture, $L_x = W_x$, or the antenna's equivalent physical width, L_ϕ. The dimensions of the imaged zone are given in range by $D_r = W_r \approx \frac{W_y}{\sin\theta_c}$ and in azimuth by $D_x = V_{SAR} T_{mes}$, with T_{mes}, the duration of the measurement, during which the scene scrolls in the ground footprint of the antenna diagram. The signal's acquisition frequency during the path of measurement trajectory is bounded by limitations related to the azimuth signal bandwidth and to the scene response spread in range, $\frac{v_{SAR}}{\delta x} \leq PRF \leq \frac{c}{2W_r}$. SAR modes, other than Stripmap, aim to improve one of the characteristics of the resulting image, mainly its azimuth resolution or the size of the imaged zone. In virtue of the physical constraints applied to SAR imaging, the improvement of a given criterion involves the deterioration of the other [MAS 08]. The use of a particular mode thus requires a set of compromises associated with certain objectives and applications. The main spaceborne SAR modes are based on the steering of the antenna beam, that is θ_c and ϕ_c are functions of x_a, the position of sensor in azimuth, made possible by using a network of active antennas.

1.3.2.3.1. Spotlight modes

During a SAR acquisition operated in *Staring Spotlight* mode, the antenna beam is mispointing with an angle ϕ_c varying with x_a, towards a fixed point, P_0, that represents the center of the imaged scene, as shown in Figure 1.38(b) [CAR 95]. The instantaneous band in azimuth, for small angles values, is nearly equal to the one measured in the Stripmap mode and that the signal obtained from an aperture $L_{x_{st\_sp}} \gg L_{x_{s_{map}}}$ can therefore be reconstructed without ambiguity with an unchanged PRF. The observation of the scene with an important aperture leads to an improvement in the azimuth resolution, $\delta x_{st\_sp} \approx \frac{L_{xs\_map}}{L_{xst\_sp}} \delta x_{s\_map}$, but with a strong reduction in the azimuthal dimension of the scene imaged, given by $D_{x_{st\_sp}} = W_x$. An intermediate solution can be found, with the *Sliding Spotlight* mode [BEL 96], illustrated in Figure 1.38(c), that proposes to steer the antenna beam towards a point P_s, located outside of the imaged scene. The sliding allows us to image the increased surface area, $D_{x_{sl\_sp}} > D_{x_{st\_sp}}$, for which

each scatterer is illuminated on an azimuthal aperture $L_{x_{st\_sp}} > L_{x_{sl\_sp}} > L_{x_{s\_map}}$. The depth of the virtual point P_s compared with the center of the scene, P_0, allows us to define the compromise between the scene's resolution and dimension in azimuth.

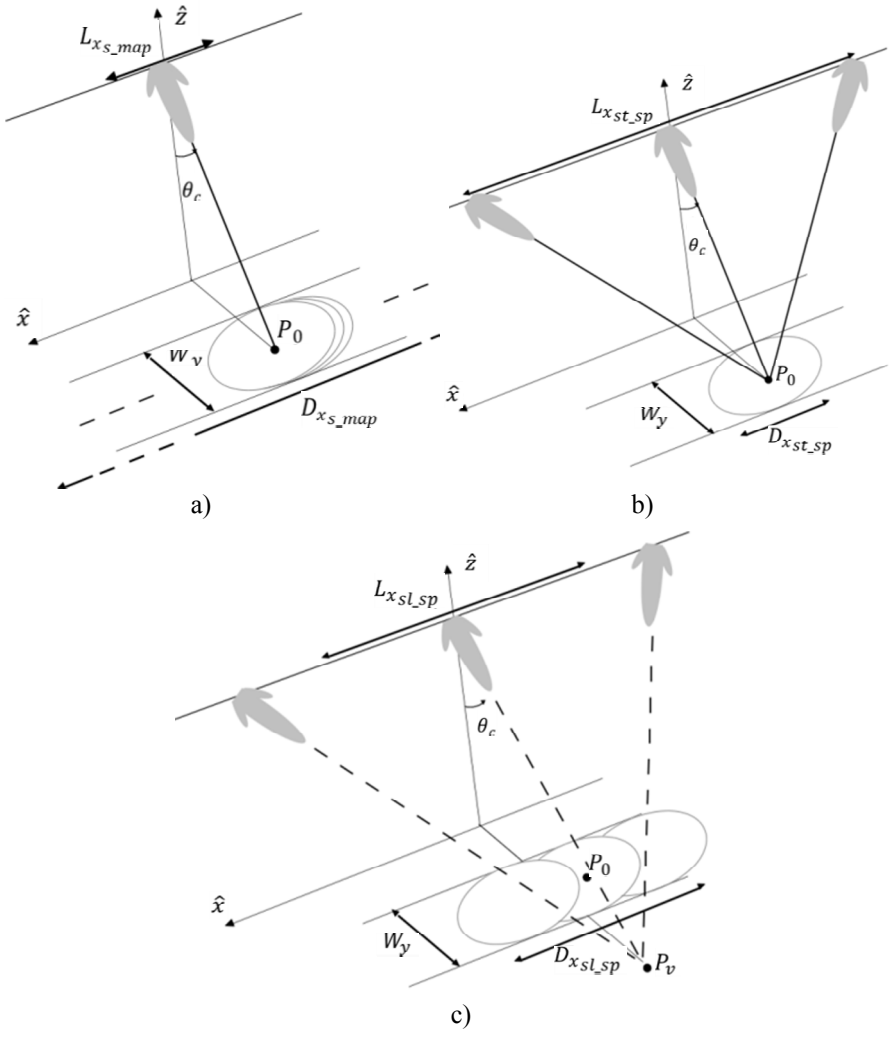

Figure 1.38. *Comparison of the geometric configurations associated to the SAR modes of: a) stripmap, b) staring spotlight, c) sliding spotlight*

1.3.2.3.2. Scan SAR mode

Even though the azimuthal dimension of an imaged scene in stripmap mode can reach very large values, fixed by the total acquisition duration T_{mes}, the dimension in range, D_r, can have a smaller value for strongly resolved systems having a very refined resolution in azimuth. This limitation in range can prove to be particularly restsrictive for the applications related to the observation of environments on a large scale. The *ScanSAR* mode [MON 96], based on a beam steering in elevation, with an angle θ_c varying with x_a, proposes a solution that allows us to image vast zones in range, as shown in Figure 1.39(a). The antenna system is steered around N_{ssw} values of the angle θ_c, corresponding to the adjacent swaths in range. A zone with the width W_x is measured in a similar manner to the stripmap mode, that is with an identical PRF, but with a reduced synthetic aperture, $L_{x_{scan}} \approx \frac{W_x}{N_{ssw}}$, before scanning the following swath in range. The substantial increase in the size of the image in range achieved through the use of N_{ssw} swaths leads to a deterioration in the azimuth resolution, with $\delta x_{scan} \approx N_{ssw}\delta x_{s\_map}$, which for the observation of a wide area is generally not problematic. The dimension of the imaged scene in azimuth is identical to the stripmap mode. The main inconvenience of this measurement mode comes from the azimuth angular diversity given by the observation over the aperture $L_{x_{scan}} < W_x$. We see, in fact, in Figure 1.39(c) that the scatterers located at different azimuthal positions are measured according to different angles ϕ and their responses are therefore affected differently by the diagram of the antenna system $G(\theta, \phi)$. This leads to a periodical modulation of the focused image amplitude, called *scalloping*, and, for angles with high $|\phi|$, a strong deterioration of the SNR. This effect is illustrated in Figure 1.40. We note that this phenomenon does not affect the stripmap mode for which each scatterer in a scene is observed over a complete angular range, $\phi \in [\phi_c \pm \frac{\phi_a}{2}]$. A ScanSAR mode variant consists of using smaller apertures, $L_{x_{scan}} \approx \frac{W_x}{N_{ssw}N_l}$, to measure using a faster scanning, each scatterer N_l times under different angles, and in combining the acquired response, with an additional deterioration of the resolution. The *TopSAR* mode [DEZ 06], or progressive scanning, is the inverse of the spotlight mode, and as shown in Figure 1.39(b), provides an efficient solution to the scalloping effect. It uses the scanSAR configuration and combines the steering in elevation, that defines the swaths in range, with a rapid azimuth steering cycle that is performed over an aperture L_{scan}. Thus, each observed scatterer has a response that is modulated during a series of bursts, by $G(\theta, \phi)$ with

$\phi \in [\phi_c \pm \frac{\phi_a}{2}]$, and not for a fixed value of ϕ, as with the ScanSAR mode. The resolution obtained and coverage are identical to those of the ScanSAR mode with $N_l = 1$.

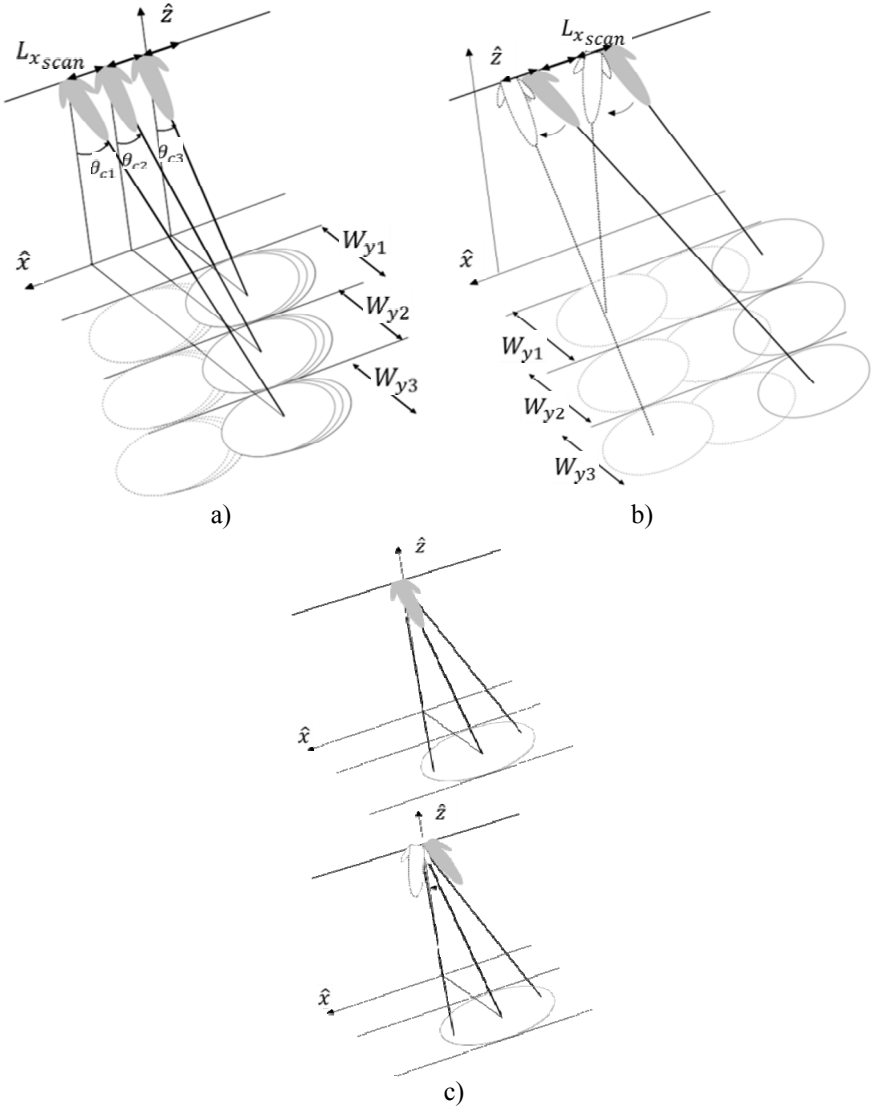

Figure 1.39. *Comparison of the SAR geometric configurations associated to scanning modes, where $N_{ssw} = 3$ and $N_l = 1$: a) ScanSAR; b) TopSAR and c) illustration of different illuminations for three points distributed in azimuth*

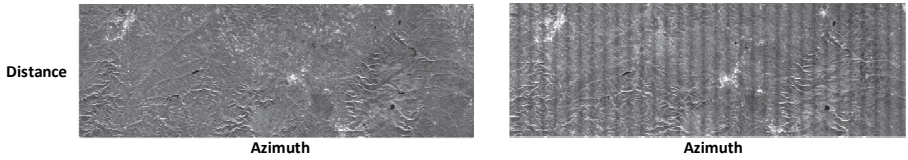

Figure 1.40. *Presentation of the scalloping effect, from [MET 10], with images taken on a swath in range and $N_l = 1$ in different modes a) TopSAR, b) ScanSAR*

The different SAR imagining modes are illustrated in Figure 1.41, for the TerraSAR-X sensor, operating in the X-band. The resolution and coverage values are constrained by the limitations previously mentioned.

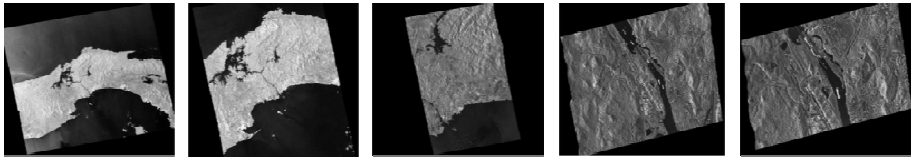

Figure 1.41. *TerraSAR-X images (from InfoTerra) of the Panama Canal region, acquired using different modes (from left to right): wide-scanSAR ($N_{ssw} = 5$, $\delta x = 40$, $Dy = 270\ km, Dx = 200\ km \leq 1\,500\ km$), ScanSAR ($N_{ssw} = 3, \delta x = 18{,}5\ m, Dy = 100\ km, Dx = 150\ km \leq 1\,650\ km$), stripmap ($\delta x = 3\ m, Dy = 30\ km, Dx = 50\ km \leq 1\,650\ km$), sliding spotlight ($\delta x = 1\ m, Dy = 5\ km \leq 10\ km, Dx = 5\ km$), staring spotlight ($\delta x = 0{,}25\ m, Dy = 4\ km, Dx = 3{,}7\ km, \theta_c = 60°$)*

1.3.3. *Correction and calibration of SAR images*

Before being used for remote sensing applications, SAR images generally have to be calibrated and corrected for certain defaults inherent to the uncertainty of measurements and their evolution during the sensor life. The objective of the calibration phase is to assure a high level of repeatability, adapted to the monitoring of small variations of the environment response or the comparison of measurements acquired by different sensors. This step is required given the complexity of the SAR systems that generally cannot be completely tested due to the aging of their different components, or due

to the changes in measuring conditions throughout time and the lack of knowledge of certain acquisition parameters that must be estimated from the signal received.

Two types of *a posteriori* SAR image corrections [JAY 14, SCH 08]:

– geometric corrections that attempt to determine, with a precision inferior to the SAR spatial resolution, the spatial location as well as the geographic correspondence between the information measured during multiple acquisitions;

– radiometric corrections aim to precisely estimate the reflectivity of an environment, by compensating for the distortions related to the used antenna system, to positioning errors and certain characteristics of the electronic components.

According to the different situations and the needs of users, we can distinguish absolute correction modes, i.e. related to physical, geometric or radiometric, stable truth or relative, i.e. using a reference point selected on an image. The characteristics used to correct an image can be estimated from the measurements:

– in the laboratory, before the use of a radar;

– during measurements that measure the transfer function of a radar system;

– after focusing over calibration targets being either passive, such as metallic manufactured objects, or active, based on transceivers for signals;

– over homogeneous distributed natural environments, with a very flat topography, for which backscattering characteristics are known in space and time.

Geometrical errors from the SAR image can be considered according to range and azimuth axes. Errors in range are mainly related to additional delays of the signal between its creation and its measurement by the radar and can be attributed to different parts of the transmitting–receiving system's characteristics, electronic components, cables, antenna system, whose

individual delay is likely to change with time, and to a lack of understating of the propagation medium, and in particular the atmosphere, for which the propagation velocity varies over time and space. These errors are generally corrected with the help of:

– an internal calibration procedure that compares a replica of the emitted baseband signal, $u(\tau)$, with versions that have traveled through the transmitting or receiving chain, $u_{TX}(\tau)$ or $u_{RX}(\tau)$, selected using couplers;

– an estimation of the antenna's orientation, ϕ_c, according to the azimuthal axis, using the measured SAR signal spectrum [MAD 89, BAM 91];

– responses of calibration targets, active or passive (Figure 1.42(a)–(b)), whose absolute coordinates are known and for which the analysis, coupled with the GPS signal processing techniques [SCH 08], allow us to estimate the residual errors as well as the propagation conditions for the traveled atmospheric path variations of the gain (Figure 1.42(c)).

Radiometric errors are mainly linked to gain variations of the radar signal's transmitting and receiving channels as well as the antenna system characteristics.

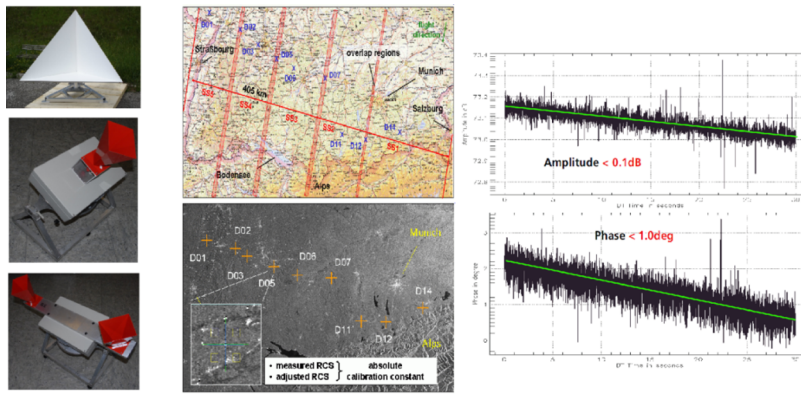

a) b) c)

Figure 1.42. *Calibration of SAR images: a) passive calibrator (above), SAR signal recorder (middle), active calibrator with transponder (below) [DOR 07], b) calibration targets deployed over several EnviSAT/ASAR ScanSAR swaths and the associated image, (images made available by the DLR), c) examples of the fast time drift of the TerraSAR-X sensor [SCH 08]*

Due to the carrier's attitude or modifications of its radiation diagram, the antenna system can present azimuth orientations and elevation, (ϕ_c, θ_c), different from the nominal values. The estimation of ϕ_c can be performed with the help of the measured signal's spectrum [MAD 89, BAM 91] on a globally homogeneous zone, from the azimuthal modulation provoked by a value of ϕ_c, different from 0. The central angle in elevation can also be estimated by modifying the antenna system's characteristics, with the inversion of the polarization of certain elements in such a manner that creates a radiation diagram, characterized by an extremely weak gain in a known direction and on a very narrow angular domain. The localization of the minimal reflectivity over a homogenous region allows us to measure θ_c with high precision (Figure 1.43(a)). Such a technique, based on the creation of a radiation diagram with a transmission, can also be applied in the azimuthal direction (Figure 1.43(b)). The radiation diagram can be estimated in the azimuthal direction, using calibration targets, passive or active, or even ground recording systems, and by taking advantage of the relationship linking the radar's position relative to the target to the angle of observation in azimuth, ϕ, with $tan\,\phi = \frac{x_0 - x_a}{r_0}$, to estimate $G(\phi, \theta_0)$ from the measured signal. The characterization of a radiation diagram in elevation is more delicate and can be done with the help of targets on the whole observed swath or with the help of a homogeneous temporarily stable zones, like the Amazonian forest, that presents an isotropic or known backscattering behavior, over a reduced angular range generally used by the SAR satellite systems [COT 11]. Once the true radiation diagram is known, it can be interpolated and compensated over the focused images. The absolute radiometric calibration is therefore obtained after the relative compensation of the previously mentioned effects and factors, with the help of several calibration targets whose reflectivity is known, and by a simple application of a compensation factor.

Here, we can note that on one hand the correction and the calibration of SAR images generally require the implementation of a set of techniques using several sources of information, combined in order to obtain a robust estimation of the system's defaults, and that on the other hand, sensors using scanning beam modes require particularly complex procedures, generally undertaken during a calibration phase, prior to the use of the measured data for remote sensing applications.

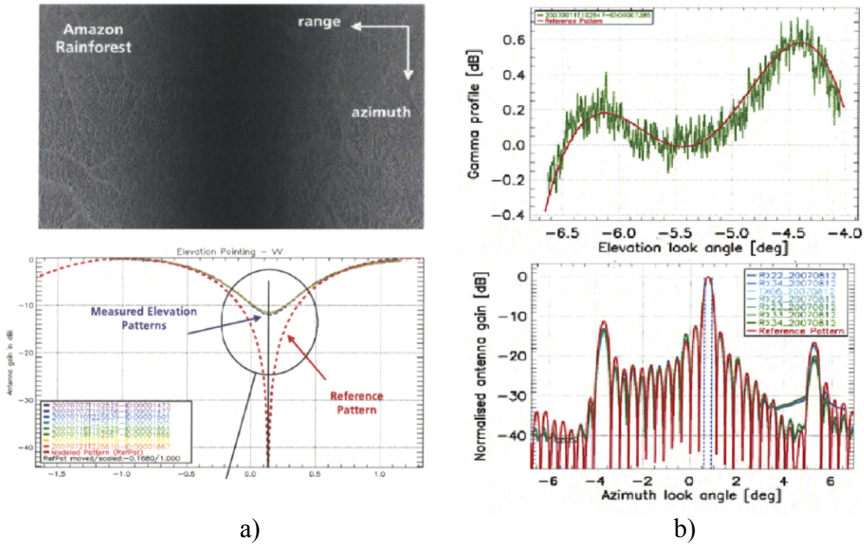

a) b)

Figure 1.43. *Calibration results of the TerraSAR-X sensor from [SCH 08]: a) the determination of the central incidence angle, θ_c, with the help of a radiation diagram with null transmission. The measured image over an Amazonian region (above), the comparison of theoretical and experimental characteristics (below), b) a radiation profile calibration in elevation, over the Amazonian site (above) and using the recorded ground signal (below)*

1.4. Key points

SAR imaging is a mapping process with high resolution of the EM reflectivity of objects or environments, based on the use of an active sensor, a radar, that transmits and receives wideband signals along a measurement trajectory. The application of an adapted bidimensional filter on the measured radar signal allows for SAR images to be focused with a significantly better resolution provided by a spectral diversity in range and spatial diversity in azimuth, increases. The process of 2D focusing using back projection consists of FFT operations and an iterative summation of the measured and compensated signals. The radiometry of SAR images can be used to measure numerous objects and environmental parameters and to quantify their temporal evolution. However, the manipulation of SAR images requires accounting for geometric distortions and the speckle effect, both of which are inherent to this mode of measurement. The importance of the speckle effect can be reduced by summation of independent realizations of the reflectivity of an environment, selected in a spatial neighborhood that is

more or less vast. The main characteristics of a SAR image are its resolution and its spatial coverage, in addition to the frequency band, incidence angle, and the emission/reception polarization of the acquired signal. The use of SAR images in remote sensing generally requires geometric and radiometric calibrations that can be performed according to procedures defined by agencies delivering the data.

1.5. Bibliography

[BAM 91] BAMLER R., "Doppler frequency estimation and the Cramér-Rao bound", *IEEE Transactions on Geoscience and Remote Sensing*, vol. 29, no. 3, pp. 385–390, 1991.

[BEL 96] BELCHER D.P., BAKER C.J., "High resolution processing of hybrid stripmap/spotlight SAR", *IEEE Proceedings on Radar*, *Sonar and Navigation*, vol. 143, no. 6, pp. 366–374, 1996.

[CAR 95] CARRARA W.G., GOODMAN R.S., MAJEWSKI R.M., *Spotlight Synthetic Aperture Radar: Signal Processing Algorithms*, Artech House Publishers, 1995.

[COT 11] COTE S., SRIVASTAVA S., MUIR S. *et al.*, "Canadian government calibration activities: assessment of distributed target sites within the RADARSAT program", *CEOS SAR Cal-Val Workshop*, 2011.

[CUM 05] CUMMING I.G., WONG F.H., *Digital Processing of Synthetic Aperture Radar Data*: *Algorithms and Implementation*, Artech House Publishers, 2005.

[CUR 91] CURLANDER J.C., MCDONOUGH R.N., *Synthetic Aperture Radar: Systems and Signal Processing*, John Wiley & Sons, 1991.

[DEG 98] DEGRAAF S.R., "SAR Imaging via modern 2D spectral estimation methods ", *IEEE Transactions on Image Processing*, vol. 7, no. 5, pp. 729–761, 1998.

[DEL 09] DELEDALLE C.A., DENIS L., TUPIN F., "Iterative weighted maximum likelihood denoising with probabilistic patch-based weights", *IEEE Transactions on Image Processing*, vol. 18, no. 12, pp. 2661–2672, 2009.

[DEL 15] DELEDALLE C.A., DENIS L., TUPIN F. *et al.*, "NL-SAR: A unified nonlocal framework for resolution-preserving PolInSAR denoising", *IEEE Transactions on Geoscience and Remote Sensing*, vol. 53, no. 4, pp. 2021–2038, 2015.

[DEZ 06] DE ZAN F., MONTI GUARNIERI A., "TOPSAR: terrain observation by progressive scans", *IEEE Transactions on Geoscience and Remote Sensing*, vol. 44, no. 9, pp. 2352–2360, 2006.

[DOR 07] DÖRING B.J., SCHWERDT M., BAUER R., "Terra SAR-X calibration ground equipment ", *Proceedings of WFMN07*, pp. 86–90, 2007.

[FER 14] FERRO-FAMIL L., "Principes de l'imagerie radar à synthèse d'ouverture", *Techniques de l'Ingénieur*, te6702, 2014.

[GOO 76] GOODMAN J.W., "Some fundamental properties of speckle", *Journal of Optical Society of America*, vol. 66, no. 11, pp. 1145–1150, 1976.

[ISH 99] ISHIMARU A., *Wave Propagation and Scattering in Random Media*, John Wiley & Sons, 1999.

[JAY 14] JAYASRI P.V., "Polarimetric SAR data processing and applications: SAR data calibration", *ISPRS TC Mid-Term Symposium*, 2014.

[KNO 74] KNOTT E.F., "The far field criterion", *Antennas and Propagation Society International Symposium*, vol. 12, pp. 92–93, 1974.

[LAS 05] LASSWELL S.W., "History of SAR at Lockheed Martin (previously Goodyear Aerospace)", *Proceedings of SPIE 5788*, *Radar Sensor Technology*, vol. 9, no. 1, 2005.

[LEC 12] LECHEVALIER F., *Principles of Radar and Sonar Signal Processing*, Artech House Publishers, 2012.

[LEE 94] LEE J.S., JURKEVICH I., DEWAELE P. *et al.*, "Speckle filtering of synthetic aperture radar images: a review", *Remote Sensing Review*, vol. 8, pp. 311–340, 1994.

[LEE 99] LEE J.S., GRUNES M., DE GRANDI M., "Polarimetric SAR speckle filtering and its implication for classification", *IEEE Transactions on Geoscience and Remote Sensing*, vol. 37, no. 5, pp. 2363–2373, 1999.

[MAD 89] MADSEN S.N., "Estimating the doppler centroid of SAR data", *IEEE Transactions on Aerospace and Electronic Systems*, vol. 25, no. 2, pp. 134–140, 1989.

[MAS 08] MASSONET D., SOUYRIS J.C., *Synthetic Aperture Radar Imaging*, CRC Press, 2008.

[MET 10] META A., MITTERMAYER J., PRATS P. *et al.*, "TOPS imaging with TerraSAR-X: mode design and performance analysis", *IEEE Transactions on Geoscience and Remote Sensing*, vol. 48, no. 2, pp. 759–769, 2010.

[MON 96] MONTI-GUANIERI A., PRATI C., "ScanSAR focusing and interferometry", *IEEE Transactions on Geoscience and Remote Sensing*, vol. 34, no. 4, pp. 1029–1038, 1996.

[OLI 04] OLIVER C., QUEGAN S., *Understanding Synthetic Aperture Radar Images*, Sci-Tech Publishing, 2004.

[OUC 13] OUCHI K., "Recent trend and advance of synthetic aperture radar with selected topics", *Remote Sensing*, vol. 5, pp. 716–807, 2013.

[ROS 04] ROSICH B., MEADOWS P.J., "Absolute calibration of ASAR Level 1 products generated with PF-ASAR", Technical note no ESA-ESRIN, ENVI-CLVL-EOPG-TN-0310, pp. 1–26, 2004.

[SCH 08] SCHWERDT M., BRAUTIGAM B., BACHMANN M. *et al.*, "Final results of the efficient TerraSAR-X calibration method", *IEEE Radar Conference*, pp. 1–6, 2008.

[SKO 08] SKOLNIK M., *Radar Handbook*, McGraw-Hill Education, 2008.

[SMA 11] SMALL D., "Flattening gamma: radiometric terrain correction for SAR imagery", *IEEE Transactions on Geoscience and Remote Sensing*, vol. 49, no. 8, pp. 3081–3093, 2011.

[SOR 06] SÖRGEL U., MICHAELSEN E., THIELE A. *et al.*, "Radargrammetric extraction of building features from high resolution multi-aspect SAR data", *IEEE IGARSS'06*, pp. 3635–3638, 2006.

[SOU 94] SOUMEKH M., *Fourier Array Imaging*, PTR Prentice-Hall, 1994.

[SOU 99] SOUMEKH M., *Synthetic Aperture Radar Signal Processing*: *with MATLAB Algorithms*, John Wiley & Sons, 1999.

[TOU 02] TOUZI R., "A review of speckle filtering in the context of estimation theory", *IEEE Transactions on Geoscience and Remote Sensing*, vol. 40, no. 11, pp. 2392–2404, 2002.

[TSA 00] TSANG L., KONG J.A., DING K.H., *Scattering of Electromagnetic Waves*, *Vol. 1: Theory and Applications*, Wiley Interscience, 2000.

[TSA 01a] TSANG L., KONG J.A., DING K.H. *et al.*, *Scattering of Electromagnetic Waves*, *Vol. 2: Numerical Simulations*, Wiley Interscience, 2001.

[TSA 01b] TSANG L., KONG J.A., *Scattering of Electromagnetic Waves*, *Vol. 3: Advanced Topics*, Wiley Interscience, 2001.

[ULA 81] ULABY F.T., MOORE R.K., FUNG A.K., *Microwave Remote Sensing: Active and Passive*, *Vol. 1*, Addison-Wesley, vol. 1, 1981.

[ULA 82] ULABY F.T., MOORE R.K., FUNG A.K., *Microwave Remote Sensing*: *Active and Passive*, *Vol. 2*, Artech House, 1982.

[ULA 86] ULABY F.T., MOORE R.K., FUNG A.K., *Microwave Remote Sensing: Active and Passive*, *Vol. 3*, Artech House, 1986.

[VAS 06] VASILE G., TROUVÉ E., LEE J.S. *et al.*, "Intensity-driven adaptive-neighborhood technique for polarimetric and interferometric SAR parameters estimation", *IEEE Transactions on Geoscience and Remote Sensing*, vol. 44, no. 6, pp. 1609–1621, 2006.

[WIL 85] WILEY C.A., "Synthetic aperture radars – a paradigm for technology evolution", *IEEE Transactions on Aerospace and Electronic Systems*, vol. 21, no. 3, pp. 440–443, 1985.